Diverse and complex muscle spindle afferent firing properties emerge from multiscale muscle mechanics

[1,2]Kyle P. Blum, [3]Kenneth S. Campbell, [2]Brian C. Horslen, [4]Paul Nardelli, [4]Stephen N. Housley, [2,4]Timothy C. Cope, [2,5]Lena H. Ting

[1]Department of Physiology
Feinberg School of Medicine
Northwestern University
Chicago, IL 60611
USA

[2]Coulter Department of Biomedical Engineering
Emory University and Georgia Institute of Technology
Atlanta, GA 30322
USA

[3]Department of Physiology
University of Kentucky
Lexington, KY 40536
USA

[4]School of Biological Sciences
Georgia Institute of Technology
Atlanta, GA 30306
USA

[5]Department of Rehabilitation Medicine
Emory University
Atlanta, GA 30322
USA

ABSTRACT

Despite decades of research, we lack a mechanistic framework capable of predicting how movement-related signals are transformed into the diversity of muscle spindle afferent firing patterns observed experimentally, particularly in naturalistic behaviors. Here, a biophysical model demonstrates that well-known firing characteristics of muscle spindle Ia afferents – including dependence on movement history, and nonlinear scaling with muscle stretch velocity – emerge from first principles of muscle contractile mechanics. Further, mechanical interactions of the muscle spindle with muscle-tendon dynamics reveal how motor commands to the muscle (alpha drive) versus muscle spindle (gamma drive) can cause highly variable and complex activity during active muscle contraction and muscle stretch that defy simple explanation. Depending on the neuromechanical conditions, the muscle spindle model output appears to "encode" aspects of muscle force, yank, length, stiffness, velocity, and/or acceleration, providing an extendable, multiscale, biophysical framework for understanding and predicting proprioceptive sensory signals in health and disease.

INTRODUCTION

Amongst the many somatosensory receptors throughout the body that give rise to our kinesthetic and proprioceptive senses, muscle spindles have a unique muscle-within-muscle design such that their firing depends critically on both peripheral and central factors. Muscle spindle sensory signals are shaped not only by the movements and forces on the body, but also by motor commands to both the muscle (alpha drive) and to specialized muscle fibers in the muscle spindle mechanosensory region (gamma drive). But, the neuromechanical interactions that lead to muscle spindle firing patterns in movement are still poorly understood. Over many decades, experimental studies of muscle spindles across several vertebrate species – from snakes to mammals and including humans – provide us with rich literature of muscle spindle firing patterns during well-controlled conditions, revealing significant nonlinearities and history-dependence with respect to muscle length and velocity (Haftel et al., 2004; Peter B. C. Matthews, 1981; Nichols & Cope, 2004; Arthur Prochazka & Ellaway, 2012; Uwe Proske & Gandevia, 2012). Moreover, manipulations to gamma motor drive reveal that muscles spindle firing patterns do not uniquely encode whole-muscle length and velocity even in tightly controlled experimental conditions (Crowe & Matthews, 1964a, 1964b; Jansen & Matthews, 1962). Independent activation of alpha and gamma motor neurons show that they can each profoundly alter muscle spindle sensory signals, rendering a direct prediction of muscle spindle signals from recordings of movement highly unlikely. Indeed, the few available recordings of muscle spindles during natural motor behaviors collectively exhibit and complex relationship(s) to the biomechanics of movement that defies simple explanation (Ellaway et al., 2015; A. Prochazka et al., 1976, 1977; Arthur Prochazka & Ellaway, 2012; Arthur Prochazka & Gorassini, 1998; A. Taylor et al., 2000; A. Taylor & Cody, 1974; Anthony Taylor et al., 2006).

Developing a mechanistic framework for understanding how muscle spindle organs generate the complex sensory signals during natural movements is critical for understanding muscle spindle sensory signals and how they change under different behaviors, in neurological disorders, and during interactions with devices or interventions to improve motor impairments. Existing computational models of muscle spindle afferent firing have largely been data-driven, with well-known experimental features with

represented phenomenologically (A Schaafsma & Willigen, 2002; Hasan, 1983; C.-C. K. Lin & Crago, 2002; Mileusnic et al., 2006). Such models have high fidelity under the conditions in which the data were collected, but generalize poorly to more naturalistic conditions. The anatomical arrangement of the muscle and muscle spindle have also been shown in simulation to affect the forces on the muscle spindle and alter muscle spindle firing properties (C.-C. K. Lin & Crago, 2002). The biomechanical properties of the intrafusal muscle fibers within the muscle spindle have also been implicated in determining muscle spindle receptor potentials (Blum et al., 2017; Fukami, 1978; Hunt & Ottoson, 1975b; Hunt & Wilkinson, 1980; Nichols & Cope, 2004; R. Poppele & Quick, 1985; U. Proske & Stuart, 1985), but intrafusal fiber forces have not been recorded experimentally in conjunction with muscle spindle afferent recordings, and only a few recordings of muscle spindle receptor potentials exist (Fukami, 1978; Hunt et al., 1978; Hunt & Ottoson, 1975b; Hunt & Wilkinson, 1980).

Here, we take a biophysical modeling approach to build a muscle spindle model based on first principles of intrafusal muscle contractile mechanics, along with its interaction with the muscle and tendon to predict both classic and seemingly paradoxical muscle spindle Ia afferent firing during passive and active conditions. We first establish a relationship between muscle spindle firing characteristics and estimated intrafusal fiber force and its first time-derivative, yank (D. C. Lin et al. 2019), in passive stretch conditions. We then build a generative model based on a simple representation of intrafusal muscle mechanics, revealing that several of classic muscle spindle firing characteristics emerge from muscle cross-bridge population kinetics. The independent effects of alpha and gamma drive on muscle spindle firing were then simulated based on mechanical interactions between the muscle spindle and the muscle-tendon unit. Highly variable muscle spindle activity observed during human voluntary isometric force generation and muscle stretch–from silent to highly active–could be explained by as a result of interactions between the muscle spindle and musculotendon unit, central activation of extrafusal (alpha drive) versus intrafusal muscle fibers (gamma drive), and muscle length change. These multiscale interactions may explain why muscle spindle activity may roughly approximate muscle force, length, velocity, acceleration, activation level, or other variables under different movement and experimental

conditions. As such, our model establishes a biophysical framework to predict muscle spindle afferent activity during natural movements that can be extended to examine multiscale interactions at the level of cell, tissue, and limb mechanics.

RESULTS

Muscle fiber force and yank reproduce diverse passive features of rat muscle spindle IFRs.

We first demonstrated that in passive stretch of relaxed rat muscle, muscle spindle Ia afferent firing rates can be described in terms of extrafusal muscle fiber force and yank. We recorded muscle spindle afferent axonal potentials and computed instantaneous firing rates (IFRs) in anesthetized rats while stretching the triceps surae muscles (Fig. 1). In the relaxed condition, i.e. in the absence of central drive to the muscles, we assumed that extrafusal muscle fiber forces provide a reasonable proxy for resistive forces of the intrafusal muscle fibers within the muscle spindle mechanosensory apparatus (Fig. 1). We previously demonstrated that whole musculotendon force in rat experiments is not predictive of muscle spindle IFRs (Blum et al., 2019), and that only a portion of the total musculotendon force can be attributed to extrafusal muscle fiber force, with the remaining nonlinear elastic component attributed to extracellular tissues (Blum et al., 2019; G. A. Meyer & Lieber, 2011; G. Meyer & Lieber, 2018). We modeled the extracellular tissue forces using a nonlinear elastic model and identified the parameters that minimized the prediction error of muscle spindle firing rates based on estimated extrafusal muscle fiber force and yank (See Methods). The initial rise in extrafusal muscle fiber force at the onset of stretch (Fig. 1, red trace) manifests as a large, transient yank signal (Fig. 1, blue trace) and became more apparent once the extracellular tissue forces were subtracted from whole musculotendon force.

Like in cats (Blum et al., 2017), fine temporal details of rat Ia afferent firing in relaxed muscles could be reconstructed by linear combinations of estimated extrafusal muscle fiber force and yank, subjected to a threshold. We assumed average extrafusal fiber force to be proportional to intrafusal muscle fiber force in the anesthetized, passive stretch condition only. The notable features of muscle

spindle Ia afferent firing reconstructed included initial bursts, dynamic responses during ramps, rate adaptation during holds, and movement history-dependent firing (Fig. 2A-C; Fig. S1). The reconstructions revealed history-dependent initial bursts in Ia afferent firing coincide with large, history-dependent yank component in estimated extrafusal muscle fiber force (Fig. 2B). The dynamic Ia afferent firing response during ramp stretches was primarily reconstructed by the force component (Fig. 2C) and was larger during the first stretch of a repeated sequence (Fig. 2B). Rate adaptation during the hold period was reconstructed by the force component in both slow and fast stretches (Fig. 2C) (P. B. C. Matthews, 1963a).

We then demonstrated that the sensitivity of Ia firing to passive muscle fiber force and yank was differentially affected by two types of perturbation to the muscle spindle afferent neuron. Estimated extrafusal muscle fiber force- and yank-based reconstruction of Ia firing rates was robust to experimental perturbations due to either oxaliplatin chemotherapy (OX) alone or intra-axonal antidromic stimulation of the afferent (STIM). While the mechanisms underlying these perturbations are undetermined, the effects on firing likely involve alterations in function of ion channels in the nerve terminal function as opposed to effects on properties of non-neural tissues, e.g. muscle. (Bullinger et al., 2011a; Cope et al., 2014; Housley et al., 2020). Accordingly, the characteristics of the estimated intrafusal muscle fiber force and yank were qualitatively similar in intact and OX rats, suggesting there was no change in muscle fiber force in the OX animals. However, muscle spindles in healthy rats treated with OX maintain an initial burst and dynamic response, but lack sustained firing during the hold period (Fig. 2D vs 2E; Fig. S2) (Bullinger et al., 2011a). These OX Ia afferent firing phenotypes were primarily reconstructed by the yank component (Fig. 2D, blue trace), with a small contribution of the force component (Fig 2D, red trace; Fig. S2), suggesting a reduced sensitivity of the muscle spindle afferent to intrafusal muscle fiber force. Conversely, when we perturbed the Ia afferent in healthy rats through intra-axonal electrical stimulation (STIM; 500 ms duration, 100 Hz train of 30nA pulses) and applied muscle stretch immediately afterward (Fig. 2F; Fig. S2), STIM Ia afferent firing phenotypes were primarily reproduced by the intrafusal fiber force, with reduced sensitivity to the intrafusal fiber yank (Fig. S3). Overall, we were able to reproduce

perturbed Ia afferent firing data by varying only the relative weighting of force and yank. Taken together, these data show that in the absence of changes in intrafusal or extrafusal muscle fiber force and yank signals, the sensitivity of the muscle spindle Ia afferent to force and yank can be decoupled and therefore may arise due to separate encoding or transduction mechanisms.

Modifying muscle spindle Ia afferent sensitivity to force and yank generates an array of firing phenotypes.

The differential effects of oxaliplatin and axonal stimulation on spindle firing rates led us to hypothesize there is a degree of independence in the transduction of force and yank in the spindle. We further tested this hypothesis by simulating Ia afferent firing arising from force- and yank-based receptor driving potentials (Fig 3A; see Methods). Nominal sensitivities of the model receptor current (closely related to driving potential) were chosen to reproduce a typical recorded muscle spindle firing rate during passive stretch (Fig 3B, green shaded box). We then generated a family of muscle spindle firing phenotypes (Fig. 3B, blue dots) by systematically varying the sensitivity of receptor currents (Fig. 3, thin black lines) to the same muscle fiber force (Fig. 3B, vertical axis) and yank signals (Fig. 3B, horizontal axis) during the same muscle stretch (Fig 3B).

Varying force- and yank- sensitivity generated diverse muscle spindle firing phenotypes similar to those observed experimentally – including the OX and STIM phenotypes. Under passive conditions, muscle spindle Ia afferent firing profiles exhibited larger initial bursts and dynamic responses as yank sensitivity increased (Fig. 3B, left to right), consistent with classically-identified dynamic muscle spindle firing phenotypes (Emonet-Dénand et al., 1977). High force sensitivity led to profiles with elevated plateau firing (Fig. 3B, top to bottom), consistent with classically-identified static muscle spindle firing phenotypes (Emonet-Dénand et al., 1977; Jansen & Matthews, 1962). The firing profiles with high yank and lowest force sensitivity resembled the OX firing phenotype (Bullinger et al., 2011a) (Fig. 3B, yellow shaded boxes, cf. Fig 2D) and the firing profiles with lowest yank sensitivity resembled the STIM firing phenotype (Fig. 3B, red shaded boxes, cf. Fig 2D). We concluded that independently varying Ia afferent

sensitivity (the input-output gain) to force and yank explains a spectrum of spindle firing phenotypes.

A muscle cross-bridge model predicts intrafusal muscle fiber force and yank underlying muscle spindle firing rates.

We next built a biophysical model of muscle spindle mechanics to more directly predict intrafusal fiber force and yank during muscle stretch conditions where experimental data are not readily available. History-dependent muscle forces have been simulated previously based on muscle cross-bridge population cycling kinetics (K. S. Campbell & Lakie, 1998; K. S. Campbell & Moss, 2000; Kenneth S. Campbell, 2014b; Kenneth S. Campbell & Moss, 2002), but no current muscle spindle model has incorporated these principles, and thus none simulate history dependence in muscles spindle Ia afferent firing (Hasan, 1983; C.-C. K. Lin & Crago, 2002; Mileusnic et al., 2006; Schaafsma et al., 1991). Muscle spindles contain bundles of specialized "bag" and "chain" intrafusal muscle fibers (Boyd, 1962, 1976; Boyd et al., 1977; M H Gladden & Boyd, 1985; A. Taylor et al., 1999). While different intrafusal muscle fibers vary morphologically and mechanically, as well as in their contributions to Ia firing patterns, their basic architectures are similar (Banks et al., 1997; Banks, 2005, 2015; M H Gladden & Boyd, 1985). Intrafusal muscle fibers are innervated by gamma motor neurons in two polar regions containing contractile muscle fibers, with an in-series non-contractile equatorial region around which the muscle spindle endings are wrapped and mechanotransduction occurs. Muscle spindle Ia receptor potentials and afferent firing are directly related to deformation of the equatorial regions (Boyd, 1976; Boyd et al., 1977), which depends on the tensile forces in intrafusal muscle fibers.

Our mechanistic muscle spindle model consists of a pair of half-sarcomere muscle models arranged in parallel, simulated using two-state actin-myosin population interactions (Kenneth S. Campbell, 2014b). The simulated "dynamic fiber" loosely represented the putative dynamic bag1 intrafusal muscle fibers, thought to mediate muscle spindle initial bursts (Banks et al., 1997; U. Proske & Stuart, 1985; Schäfer & Kijewski, 1974; Schäfer & Schäfer, 1969; Song et al., 2015). The simulated

168 "static fiber" loosely represented the bag2 and chain intrafusal muscle fibers of the muscle spindle
169 thought to mediate tonic muscle spindle firing (Fig. 4A) (R. E. Poppele et al., 1979). The dynamic fiber
170 model was designed with slower myosin attachment rates (Thornell et al., 2015b) and with a more
171 compliant passive element than the static fiber (Margaret H. Gladden, 1976) (see Methods; Fig. S5).
172 Length changes to the spindle were applied to both fibers equally. We assumed the receptor driving
173 potential of the Ia afferent receptor ending to be proportional to a weighted combination of force and yank
174 of the intrafusal fibers based on visual inspection of intrafusal force recordings and our previous
175 hypotheses of intrafusal force and yank encoding (Blum et al., 2019; Fukami, 1978; Hunt & Ottoson,
176 1975b). This was based on the idea that the intrafusal mechanosensory nuclear regions stretch linearly
177 with intrafusal force (Peter B. C. Matthews, 1981; Schaafsma et al., 1991) and do not themselves
178 contribute significantly to the force profile of the intrafusal muscle fiber (Fig. 4A, lower panel; See
179 Materials and Methods for more details).

180 Our mechanistic model predicted a spectrum of muscle spindle firing phenotypes identified in
181 passive stretch conditions by varying the sensitivity (gain) of driving potentials to biophysically-predicted
182 intrafusal fiber force and yank (Fig. 4B). The predicted muscle spindle firing phenotypes closely
183 resembled biological firing phenotypes discussed earlier. As a result of our chosen kinetic scheme,
184 history-dependent forces emerge within our simulated intrafusal muscle fibers from cross-bridge
185 population dynamics (Fig 4C). When the muscle is at rest, the spontaneous formation and breakage of
186 cross-bridges is at steady-state equilibrium (Fig. 4C, time 1). As soon as a stretch as applied, the
187 population of attached cross-bridges is also stretched, resulting in a short period of high-stiffness force
188 response, known as short-range stiffness (Fig. 4C, time 2; Lakie and Campbell 2019). Once these cross-
189 bridges are stretched to their limits, they break and a new attachment equilibrium is reached during the
190 remainder of stretch (Fig. 4C, between times 2 and 3). If the muscle is shortened back to the original
191 length, the cross-bridges will shorten (Fig. 4C, time 4 – note the distributions shift leftward). In this case,
192 the force in the fibers will decrease until the fibers are slack (Fig. 4C, time 5), at which point the cross-
193 bridges will shorten the muscle fibers against zero load until the slack length is reduced to zero, or

another stretch is applied (Fig. 4C, time 6). If the fibers are not given enough time to return to steady-state equilibrium (e.g., Fig. 4C, time 1), a stretch will result in qualitatively different, history-dependent force and yank responses.

A biophysical muscle spindle model predicts a variety of classic muscle spindle firing phenomena.

A truly general model of a muscle spindle would predict firing properties across different experimental contexts without any fundamental changes to the model structure or parameters. Using a single, nominal set of parameters in our muscle spindle model, we tested whether a variety of classical muscle spindle firing characteristics during passive stretch would emerge, including: fractional power relationship with stretch velocity (P. B. C. Matthews, 1963a), history-dependence (Haftel et al., 2004), and increased firing due to gamma motor neuron activation (Boyd et al., 1977; Crowe & Matthews, 1964a, 1964b). To demonstrate the ability of the mechanical signals themselves to predict the properties observed in Ia afferent firing rates, we examined simulated driving potentials rather than creating additional degrees of freedom in our model with a spike generating process.

In our model, the scaling properties of muscle spindle dynamic responses and initial bursts with increasing velocity during passive muscle stretch arise from intrafusal cross-bridge kinetics. More specifically, the strain dependence of the cross-bridge detachment rates produces force profiles that contain linear increases in short-range stiffness and sublinear increases in force dynamic response as a function of stretch velocity. In a series of constant velocity stretches relative to optimal muscle length, L_0 (0.1 - 1.0 L_0/s in 0.1 L_0/s increments; Fig 5A), we computed the "dynamic index", classically defined as the difference in firing rate between the end of the ramp and after 0.5 s of isometric hold, which increases with stretch velocity (Fig. 5B-C; P. B. C. Matthews 1963a). We predicted a sublinear increase in dynamic index with stretch velocity, emergent from intrafusal mechanics, resembling the classically-reported fractional-power velocity relationship in muscle spindle firing rates (Fig. 5C Houk, Rymer, and Crago 1981). In the same simulations, linear scaling of initial burst amplitude with stretch acceleration was predicted (Schäfer & Kijewski, 1974; Schäfer & Schäfer, 1969). Initial burst scaling was emergent from

intrafusal muscle fiber yank at the onset of stretch due to the elasticity of attached cross-bridges that then detach rapidly after being stretched a small fraction of L_0 (Hasan & Houk, 1975; P. B. Matthews & Stein, 1969). To our knowledge, neither of these phenomena has been previously demonstrated to arise from the same mechanistic model.

Our biophysical model predicted history-dependent changes in the muscle spindle firing initial burst and dynamic response analogous to those previously reported in acute cat, rat, and toad experiments as well as in microneurographic recordings in awake humans (Blum et al., 2017; Day et al., 2017; Haftel et al., 2004; U. Proske & Stuart, 1985). In our model, these features emerged from the asymmetry present in strain-dependent cross-bridge detachment rates. In three consecutive, identical stretches, the biophysical muscle spindle model predicted an initial burst and elevated dynamic response on the first, but not second stretch (Fig. 6A). In the third stretch, the amplitude of the simulated driving potentials recovered asymptotically as the time interval between stretches increased to 10s (Fig. 6A), resembling the recovery of spike counts during the dynamic response in rats (Fig 6B) (Haftel et al., 2004) and the recovery of initial bursts as a function of hold period in toads (Fig. 6B; Proske and Stuart 1985). Our model predicted an initial burst at the onset of sinusoidal muscle stretches (Fig. 6C), similar to that seen in microneurographic recordings from awake humans (Fig. 6C; Day et al. 2017). Although a cross-bridge mechanism has been proposed previously based on experimental findings (Haftel et al., 2004; Nichols & Cope, 2004; U. Proske et al., 1992; U. Proske & Gregory, 1977; U. Proske & Stuart, 1985), this is the first demonstration of history dependence in a muscle spindle model.

A biophysical muscle spindle model predicts effects of gamma drive on muscle spindle firing.

We tested whether previously-reported effects of gamma motor neuron activity on muscle spindle afferent firing characteristics during passive muscle stretch conditions were also emergent from our biophysical model. Dynamic and static gamma motor neurons innervate the static and dynamic intrafusal muscle fibers within the muscle spindle, respectively. To simulate classic experiments in which dynamic and static gamma motor neurons were electrically stimulated in anesthetized animals, we independently

increased the number of available actin binding sites in simulated intrafusal static and dynamic muscle fibers (Fig. 7A). Consistent with many prior experimental findings, simulated dynamic gamma drive increased the force and yank of the dynamic fiber during stretch, predicting increased receptor driving potentials underlying initial burst and dynamic responses, with proportionately smaller increases in baseline muscle spindle driving potentials (Boyd et al., 1977; Hunt & Wilkinson, 1980). In contrast, simulated static gamma drive primarily increased baseline muscle spindle driving potentials, and had much smaller effects on driving potentials underlying the initial burst and dynamic response during stretch (Fig. 7A-B; Crowe and Matthews 1964a; Boyd et al. 1977; Crowe and Matthews 1964b). Even the previously-reported increases and decreases in dynamic index as a result of dynamic versus static fiber stimulation, respectively, (Fig. 7C left plot; Crowe and Matthews 1964a; 1964b) were predicted by our model (Fig. 7C right plot).

Interactions between a biophysical muscle spindle model and muscle-tendon dynamics predict paradoxical muscle spindle firing in isometric force production

To simulate how alpha and gamma drive affect muscle spindle Ia afferent firing during voluntary movement, we simulated the peripheral mechanical interactions of the biophysical intrafusal muscle fiber above within extrafusal muscle-tendon dynamics. We modeled the muscle spindle and extrafusal muscle-tendon dynamics while the total end-to-end length was held constant to simulate isometric muscle contractions(Dimitriou, 2014; Edin & Vallbo, 1990) (Fig. 8). All of the force on the tendon was generated by the extrafusal muscle fibers, as the intrafusal muscle fiber was assumed to generate negligible force. We constrained the end-to-end lengths of the intrafusal and extrafusal muscle fibers to be the same. However, muscle fibers were allowed to go slack based on their own properties, meaning the true fiber lengths were not necessarily equal when slack was present in one or more fibers. Alpha drive was simulated by activation of the extrafusal muscle fiber and gamma drive was simulated by activation of the intrafusal muscle fiber (Fig. 8A).

We first tested the individual effects of alpha and gamma drive by independently activating extrafusal and intrafusal muscle fibers in gaussian activation patterns (Fig. 8B, first two columns). When extrafusal muscle was activated to 50% with intrafusal activation at a nominal constant level, the stress in the extrafusal fiber increased, while the stress in the intrafusal fiber decreased (Fig. 8B, first column, top trace, purple and green traces, respectively). The Ia afferent firing rate simulated using an integrate-and-fire neuron was abruptly silenced during extrafusal muscle contraction (Fig. 8B, first column, middle trace); during this condition both the extrafusal and intrafusal muscle lengths decreased and tendon length increased (Fig. 8B, First column, bottom trace, green-purple vs. orange trace). Here, the extrafusal muscle shortens due to the simulated alpha drive, and the intrafusal muscle fiber goes slack, causing a decrease in intrafusal fiber stress. In contrast, when intrafusal fiber activation (both static and dynamic) was increased and extrafusal activation was held constant, we observed no change in extrafusal stress or force, but an increase in intrafusal stress (Fig. 8B, first column, top trace, purple and green traces, respectively). The increase in intrafusal stress causing an increased in simulated Ia afferent firing rate (Fig. 8B, second column, middle trace) with no change in muscle fiber or tendon length (Fig. 8B, second column, bottom trace).

When we simulated concurrent alpha and gamma drive, we observed Ia afferent firing that was dependent on the relative balance of imposed shortening of intrafusal fibers by alpha drive and the activation of intrafusal fibers by gamma drive (Fig. 8B, third and fourth columns). As a proof of concept, we activated the intrafusal and extrafusal fibers at a “low” and “medium” level, respectively (Fig. 8B, third column, top trace), which caused an increase in extrafusal muscle fiber stress, a decrease in intrafusal muscle fiber stress (Fig. 8B third column, top trace, purple and green traces), and a termination of Ia afferent firing (Fig. 8B, third column, middle trace), while both extrafusal and intrafusal muscle fiber lengths shortened (Fig. 8B, third column, bottom trace). Here, the extrafusal shortening due to alpha drive outweighed the effects of gamma drive to the intrafusal muscle fiber and silenced the Ia afferent (Fig. 8B, third column). When we reversed the relative activations so intrafusal activation was “medium” and extrafusal activation was “low”, both intrafusal and extrafusal muscle fiber stress was increased while

the muscle shortened (Fig. 8B, fourth column, top versus bottom traces), causing increased Ia afferent firing (Fig. 8A, fourth column, middle trace). In this case, both extrafusal and intrafusal muscle fibers were shortening, but the presence of adequate intrafusal activation maintains the force in the intrafusal muscle fibers, driving the muscle spindle firing in the presence of alpha drive to the extrafusal muscle fiber (Fig. 8B, fourth column).

The simulations just described illustrate the multiscale, complex, interactions between the musculotendon and the muscle spindle in a few intuitive cases (Fig. 8C-E). Briefly, if the extrafusal muscle shortening caused by alpha motor drive is not sufficiently counteracted by gamma drive, the Ia afferent will reduce its firing rate or cease firing altogether (Fig. 8C). Alternatively, if the gamma drive to the spindle stretches the sensory region at a greater rate than the extrafusal shortening, the Ia afferent will increase its firing rate (Fig. 8D). Finally, it follows that there is a set of extra- and intrafusal states that will lead to no change in Ia firing rate during isometric conditions (Fig. 8E).

We were inspired to use these observations to explain paradoxical Ia afferent firing rates from experiments in human finger muscles (Fig. 8C; Edin and Vallbo 1990), in which muscle spindle Ia afferents were shown to either increase or decrease their firing rates (Fig. 8C, bottom traces) during an isometric contraction despite the same joint torque profile (Fig. 8C, top traces). We mimicked muscle fiber shortening under isometric conditions by applying a ramp increase in extrafusal muscle activation (Fig. 8D). As expected, increasing alpha drive decreased extrafusal muscle fiber length (Fig. 8B, black trace), and increased extrafusal muscle fiber stress (Fig. 8D, purple trace). In the absence of gamma drive, the intrafusal fiber stress decreased as alpha drive increased (Fig. 8D, green trace) resulting in no muscle spindle firing as shown experimentally (Elek et al., 1990). When we increased gamma drive by a fixed amount intrafusal fiber stress could increase (Fig 8D, pink traces), decrease (Fig 8D, green traces), or experience no change (Fig 8D, purple traces) in stress depending on the amount of alpha drive. As such it was possible to generate almost any level of muscle spindle firing during isometric conditions where the muscle fibers shorten by varying the relative levels of alpha and gamma drive.

Finally, to demonstrate the complex interplay of alpha and gamma drive when muscle fibers are lengthened, we applied ramp-and-hold stretches to the model musculotendon while simulating the Ia afferent response under different extra- and intrafusal activation conditions. When the musculotendon was passive, i.e. no alpha drive, the muscle fiber length closely followed the applied musculotendon length (Fig. 9A, left panel). Conversely, when the extrafusal muscle fiber was activated during the stretch, there was a marked difference in musculotendon length compared to the applied length (Fig. 9A, right panel). For each of these cases, we simulated muscle spindle Ia afferent responses with and without gamma drive. In the case of the passive spindle, the musculotendon stretch in the absence of alpha drive produced a slightly higher muscle spindle Ia afferent response than in the presence of alpha drive (Fig. 9B, top row). Specifically, the baseline firing rate, initial burst, and dynamic response were all slightly larger in the case of the passive musculotendon. These differences were more exaggerated when we simulated gamma drive by increasing intrafusal muscle fiber activation (Fig. 9B, bottom row). The addition of a tonic level of gamma drive increased the baseline firing rate, the amplitude of the initial burst, and the dynamic response to stretch in the passive extrafusal musculotendon unit (Fig. 9B bottom row, green trace). Adding alpha drive decreased baseline firing only slightly, abolished the initial burst, and had little effect on the dynamic response to stretch (Fig. 9B bottom row, purple trace). These simulations demonstrate the importance of considering musculotendon dynamics and activation when estimating muscle spindle afferent feedback in different experimental conditions.

DISCUSSION

Summary

Here, we present a multiscale biophysical model that predicts a wide range of muscle spindle Ia afferent firing characteristics in both passive and active conditions, illustrating the complex central and peripheral neuromechanical interactions that underlie them in naturalistic conditions. We demonstrated that a diverse range of Ia afferent firing characteristics during passive stretch – well-documented in the literature but not completely understood mechanistically – is emergent from first principles of intrafusal muscle contractile

(cross-bridge) mechanisms. Ia afferent firing in a broad range of behaviorally relevant conditions can be reproduced by converting the force and yank of the intrafusal muscle fibers within the muscle spindle into afferent driving potentials using a simple linear relationship. This transformation represents the yet unexplained mechanotransduction process in the equatorial encoding region of muscle spindle sensory organs. The multiscale mechanical interaction of the muscle spindle within the muscle tendon unit revealed isometric force generating conditions in which muscle spindle firing followed intrafusal muscle fiber force, which can either resemble or differ from muscle-tendon unit force or length depending on the relative amounts of alpha and gamma motor neuron drive. As such, mechanical interactions within the muscle-tendon unit and forces external to the muscle all contribute to firing rates of muscle spindle Ia afferents; they may even create firing patterns considered to be paradoxical if viewing muscle spindles as simple passive sensors of kinematic or kinetic variables. Finally, we simulated multiscale mechanical interactions including movements, alpha activation of extrafusal muscle, and gamma activation of intrafusal muscle to demonstrate the importance of these complex interactions when modeling proprioceptive activity. Our neuromechanical framework demonstrates how muscle spindle firing can reflect the complex interplay of external and self-generated forces and motion. Importantly, our model provides a foundation for biophysically realistic, predictive muscle spindle models that can be extended to understand how properties of tissues, muscles, neurons, and central drive affect muscle spindle sensory function in health and disease.

A biophysical muscle model connects many independent observations with a simple hypothesis

Our approach of starting with biophysical principles of muscle force generation enabled us to develop a muscle spindle model that predicts nonlinear muscle spindle firing properties beyond the conditions that it was designed to replicate, without any change in model parameters. We simulated muscle cross-bridge kinetics to produce the muscle fiber force and yank that drive history-dependent responses to a repeated muscle stretch stimulus, including the initial burst. Other muscle spindle models do not exhibit history-dependence and – by design – either lack (Mileusnic et al., 2006) or always

generate (Hasan, 1983) an initial burst at the onset of stretch. In our model, the initial burst emerges from the number of cross-bridges that are formed after a period of rest, temporarily increasing the stiffness of the fibers before being stretched to their mechanical limit. This number depends on the prior and current fiber length, velocity, acceleration, and activation of the intrafusal fibers, and thus leads to the modulation of the initial burst of the spindle afferent with these variables. Similarly, the fractional power relationship between muscle spindle dynamic responses and stretch velocity (Hasan, 1983; C.-C. K. Lin & Crago, 2002) has previously been imposed by including it explicitly within the model definition. While it can be simulated using a phenomenological muscle model with a built-in fractional power function, prior models fail to account for the history dependence of the velocity sensitivity and thus fail to replicate muscle spindle firing patterns outside of tightly controlled laboratory conditions. Similarly, the adaptation of muscle spindle firing rates when held at a constant length after stretch follows the decrease in force of the intrafusal muscle fiber when it is held at a constant length (Blum et al., 2017; Husmark & Ottoson, 1971). Here, history dependence, the nonlinear relationship to stretch velocity, the scaling of the initial burst to acceleration, and firing rate adaptation are all implicit, emergent properties of intrafusal cross-bridge force and yank under different conditions – no explicit formulation of these relationships is necessary.

Even the apparent differential effects on Ia afferent encoding by static and dynamic fusimotor activity are accounted for by the mechanics of muscle force generation (Crowe & Matthews, 1964a, 1964b). We designed our model with slow cycling myosin in the “dynamic” fiber and fast cycling myosin in the “static” fiber, modeled after nuclear bag and chain fibers, respectively (Thornell et al., 2015b). In doing so, the dynamic and static fusimotor effects on Ia afferent stretch sensitivity were closely predicted, emerging from muscle biophysics and a simple representation of mechanotransduction (Banks et al., 1997). By taking a structural approach to the interactions between intrafusal and extrafusal muscle fibers the effect of gamma motor drive were more robustly simulated (C.-C. K. Lin & Crago, 2002).

Variations in force and yank sensitivity account for both overall firing characteristics as well as “static-dynamic” variability across Ia afferents during passive stretch. The few available recordings of muscle spindle receptor potentials during muscle stretch exhibit fast initial transients similar to muscle

fiber yank, as well as a sustained potential that resembles muscle force and its decay following a stretch (Hunt & Ottoson, 1975a). We show that sweeping a range of sensitivities to intrafusal force and yank predicts a continuum of firing phenotypes resembling those seen previously in both healthy and perturbed conditions (Housley et al., 2020; Vincent et al., 2016). Further, each set of sensitivities can predict muscle spindle firing across different stretch velocities and displacements. Whether a similar principle describes the firing of the second type of muscle spindle afferent, group II afferents, remains to be tested.

Multiscale interactions are necessary to consider for natural behavior

Explicit simulation of the mechanical arrangement of the intrafusal muscle fibers within the muscle-tendon unit enabled us to demonstrate the profound effects that central drive to alpha and gamma motor neurons can have on muscle spindle firing during active force and muscle stretch conditions. Our work emphasizes the importance of modeling the anatomical arrangement of the muscle shown in some prior models (C.-C. K. Lin & Crago, 2002; Mileusnic et al., 2006). With the addition of biophysical force generation mechanics we now provide a computational testbed to better explore the long-discussed idea that muscle spindle firing rates are driven by properties of intrafusal muscle fiber forces (Peter B. C. Matthews, 1981), and determined by both the central drive to intrafusal and extrafusal muscle fibers, as well as interactions with external forces on the muscle. When simulating the mechanical interaction of the muscle spindles within the muscle tendon unit, our model reveals that muscle spindle firing can depend critically on the activation, force, and length of the intrafusal fiber within the muscle spindle, which shapes the degree to which muscle spindle firing resembles extrafusal muscle length, velocity, force or other biomechanical variables (Bewick & Banks, 2015; Kruse & Poppele, 1991).

The multiscale model presented here provides a mechanistic framework that can explain the rich diversity of movement-related biomechanical signals in naturalistic behaviors. There are many such scenarios we have not simulated that our model may provide insights for. For example, the mechanical interactions between intrafusal and extrafusal muscle fibers (Fig. 8, 9) may explain the complex relationships between Ia afferent signals in locomotion to muscle length and force. During the swing

425 phase of the cat locomotor step cycle, relaxed ankle extensor muscles are stretched by activity in ankle
426 flexor muscles, and extensor Ia firing rates appear to follow muscle velocity and/or length (A Prochazka
427 & Gorassini, 1998; Arthur Prochazka & Gorassini, 1998), which closely resemble extrafusal and
428 intrafusal muscle force and yank (Blum et al., 2017) in passive conditions. However, the same muscle
429 spindle Ia afferent also fires in early stance when there is no change in muscle length, but the muscle is
430 both active due to alpha drive, and loaded due to the carrying the weight of the animal: this firing is likely
431 due to intrafusal force resulting from the interactions between gamma drive, alpha drive, and the external
432 load (Fig. 8, green traces). The same muscle spindle afferent ceases firing in midstance, when the
433 intrafusal muscle is possibly activated by gamma drive, but not enough to prevent the muscle spindle
434 from falling slack as the extrafusal muscle fiber shortens due to alpha drive (Ellaway et al., 2015; Arthur
435 Prochazka, 2015; Arthur Prochazka & Gorassini, 1998) (Fig. 8, purple traces). We did not simulate such
436 experiments, but doing so would provide an excellent opportunity to further improve our framework for
437 natural movements.

438 Complex biomechanical interactions may further explain muscle spindle afferent activity that
439 have heretofore proven challenging model and to understand mechanistically. Ia afferent firing has been
440 shown in humans to be highly dependent on resistive loads applied to an attempted movement (Dimitriou,
441 2014; Edin & Vallbo, 1990; Vallbo, 1974). An interpretation of this observation could be that, in coupled
442 agonist-antagonist systems, Ia afferents under alpha-gamma coactivation or beta motor control signal the
443 effects of loads on a joint originating outside their parent muscles. For example, in an unimpeded
444 concentric contraction, the antagonist Ia afferent stretches and signals the effect on the joint torque and
445 angle caused by the agonist contraction. If, in a similar scenario, a load prevents the agonist from
446 shortening, there would be no change in the antagonist Ia afferent activity, correctly signaling the lack of
447 joint movement. Simultaneously, the agonist Ia afferents would increase their firing due to concomitant
448 fusimotor drive, signaling the impeding effects of the external load on the joint. In both cases, the Ia
449 afferent, whether in an agonist or antagonist muscle, would fire when interacting with a force that
450 originates outside the parent muscle. Whether the antagonist load or reciprocal inhibition of the fusimotor

drive between antagonist muscle pairs explains these results, Ia afferents in opposing muscles may work together to signal joint-level information about external loads (Dimitriou, 2014). Simulating such intermuscular interactions is likely necessary to predict proprioceptor activity during movement, and would require multiple muscle and muscle spindle models to be coupled.

Limitations of our current model and future directions

The core framework presented provides proof of concept for more elaborate and biophysically accurate model of muscle spindle firing necessary to predict muscle spindle signals during naturalistic movement conditions in health and disease. Importantly, our model can be used as a platform to enable the development of computational models capable of testing the effects of a wide variety of multiscale mechanisms on muscle spindle firing, including architectural arrangement of the muscle spindle within the muscle (Maas et al., 2009), intra- and extrafusal muscle myosin expression, more complex muscle force-generating mechanisms, extracellular matrix stiffness, mechanosensory encoding mechanisms, and biophysical neural dynamics that could all be affected by aging and disease.

Our primary focus in developing our mechanistic model was to use the simplest two-state cross-bridge model of actin-myosin interactions to qualitatively, but not quantitatively, reproduce history dependence in its stretch responses (Figure 6A) as seen in biological Ia afferents (Figure 2B). It should be noted that, despite the discrepancies in the more abrupt stretch-shorten “triangle” stretches (Figure 6A), our model was able to closely reproduce the human Ia afferent response (Figure 6B, C) during the slow sinusoidal stretch, which may be more physiologically relevant. However, we acknowledge the apparent shortcomings of our chosen model in reproducing the triangle responses from anesthetized rat. With our approach, it is impossible to separate the elastic contributions from endomysial tissue from those in myofilaments, from structures such as titin. It remains to be seen which aspects of complex muscle spindle properties will improve the model’s predictive capabilities, but it may be necessary to account for muscle-specific (Kenneth S. Campbell, 2014b) kinetic schemes or to replace the simple linear model of titin with more sophisticated properties (Nishikawa et al., 2012) to capture calcium-dependent hysteresis

in regulation of titin stiffness and a range of other complex processes of muscle force generation (Kenneth S. Campbell, 2016, 2017; Mann et al., 2020). We relied on the similarly timed short-range elastic component of extrafusal force response to predict the putative intrafusal mechanics-driven Ia afferent stretch responses. Additional sources of history-dependence could include history dependence in extrafusal muscle fibers and non-contractile tissues, or the inertial of the muscle mass when rapidly accelerated. Another possibility is that we failed to account for the complex process(es) responsible for the occlusion between multiple transduction zones in the primary afferent (Banks et al., 1997; Mileusnic et al., 2006), in which the firing rate may be more dependent on the bag1 fiber during the initial stretch and become more dependent on to bag2 and chain fibers in later stretches.

A comprehensive understanding of the mechanisms underlying muscle spindle mechanotransduction, i.e. translation of mechanical stimuli to receptor potentials, remains elusive. Lacking sufficiently detailed information from the literature, we represented the entire neuromechanical transduction process by a set of constant gains. However, we do recognize that the dynamics of yet uncharacterized viscoelastic properties of the equatorial regions of intrafusal muscle fibers, ion channels in muscle spindle afferent endings (Bewick & Banks, 2015; Carrasco et al., 2017), and intrinsic neural dynamics (e.g. those underlying neural history dependence, spike-frequency adaptation, and occlusion Banks et al., 1997) of the afferent plays a significant role in the resulting muscle spindle firing signals. Finally, we focused only on the muscle spindle Ia afferent, but the anatomical arrangement of our model could also provide a biophysical framework for understanding muscle spindle group II afferents that are located at the junction between the polar and equatorial regions of intrafusal muscle fibers, as well as and Golgi tendon organ Ib afferent located at the extrafusal musculotendinous junction. In future studies, it would also be beneficial to adopt the approach of Mileusnic and colleagues (Mileusnic et al., 2006) and optimize the parameters of our model to match the careful experimental conditions of specific muscles and animal models.

Conclusion

Ultimately, it is clear that the complex interplay between central drive, internal, and environmental forces cannot be ignored when decoding muscle spindle firing patterns, especially in voluntary movement and during interactions with the environment. Such neuromechanical interactions are key in interpreting the afferent signals and percepts in a variety of conditions where mismatches in extrafusal and intrafusal mechanical state due to fatigue or pre-conditioning alter the perception of both force and position (Uwe Proske et al., 2014; Uwe Proske & Gandevia, 2012), or the role of muscle spindles in perception of force and weight (Jami, 1992; Luu et al., 2011; Savage et al., 2015). Our multiscale biophysical model provides a new platform by which we may move beyond the idea that muscle spindles can be characterized as simple passive encoders of biomechanical signals during movement enabling a more sophisticated understanding of muscle spindles as proprioceptive sensors, their role in neural control of movement, and how neurological disorders disrupt sensorimotor systems.

FIGURES

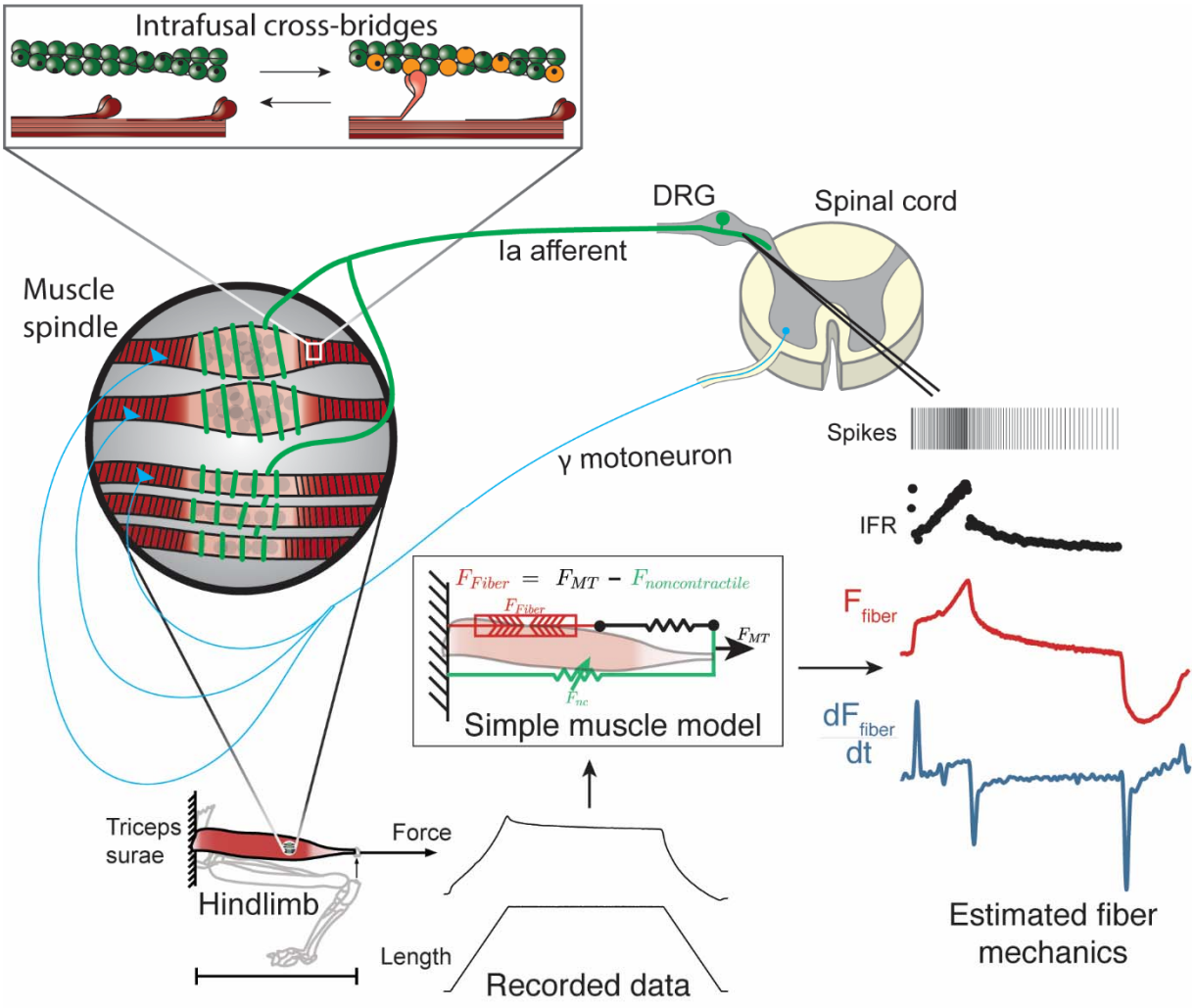

Figure 1 Overview of methodologies to test hypothesis that muscle spindle Ia afferent firing rates follow intrafusal muscle fiber force due to cross-bridge interactions. Ia afferent firing rates were recorded from dorsal rootlets during stretches of the triceps surae muscle in anesthetized rats. Muscle fiber forces were estimated by subtracting noncontractile forces from measured whole musculotendon force. The exponential rise in force with stretch was assumed to arise from non-contractile tissue in parallel with the muscle-tendon unit with exponential stiffness (Blum et al. 2019). The remaining estimated muscle fiber force and yank exhibited similar temporal characteristics to the muscle spindle IFR. Intrafusal muscle fiber force and yank were then simulated using a cross-bridge based model to predict muscle spindle IFRs.

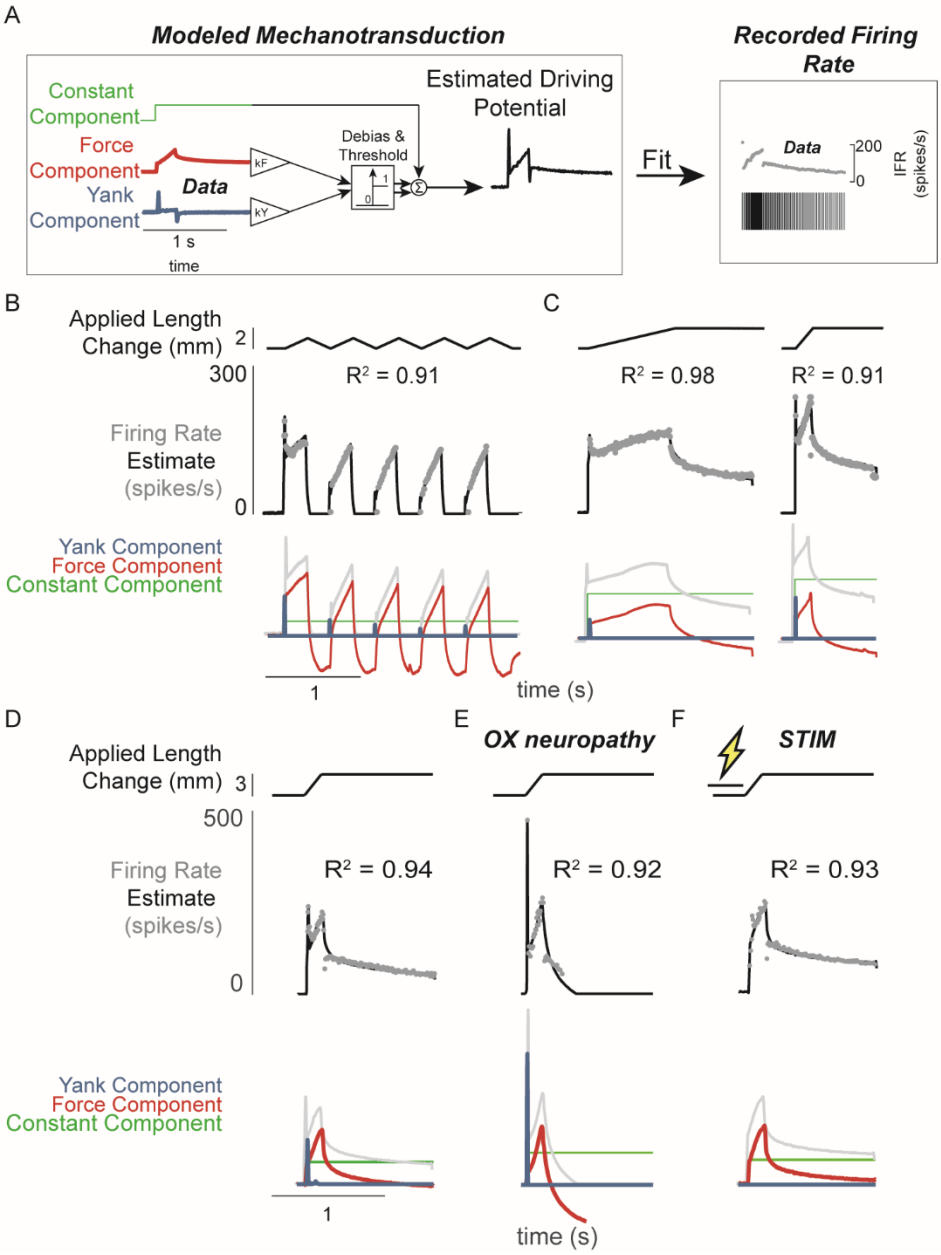

Figure 2 Muscle spindle driving potentials estimated from independent contributions of experimentally-derived muscle fiber force and yank. A) Estimated driving potentials were derived from linear combinations of muscle fiber force and yank, half-wave rectified, and compared against recorded muscle spindle Ia afferent firing rates. Weights of each component were optimized to match recorded spiking dynamics. B) Recorded muscle spindle Ia afferent firing rates (gray dots) in history-dependent conditions, having non-unique relationships to muscle length and velocity, were reproduced using muscle fiber force and yank (black lines). Notably, the initial burst and increased firing during ramp in the first stretch were attributed to increased muscle fiber yank and to greater force during the first stretch, respectively. C) Likewise, muscle fiber force and yank could also account for the temporal dynamics of Ia afferent firing in response to both slow and fast stretches. D) This model permits independent manipulation of the force and yank contributions to muscle spindle firing rates. As such, we can

explain the altered muscle spindle Ia afferent firing patterns in E) oxaliplatin chemotherapy-induced sensory neuropathy as a loss of force sensitivity, and F) after antidromic electrical stimulation of the axon as loss of yank sensitivity.

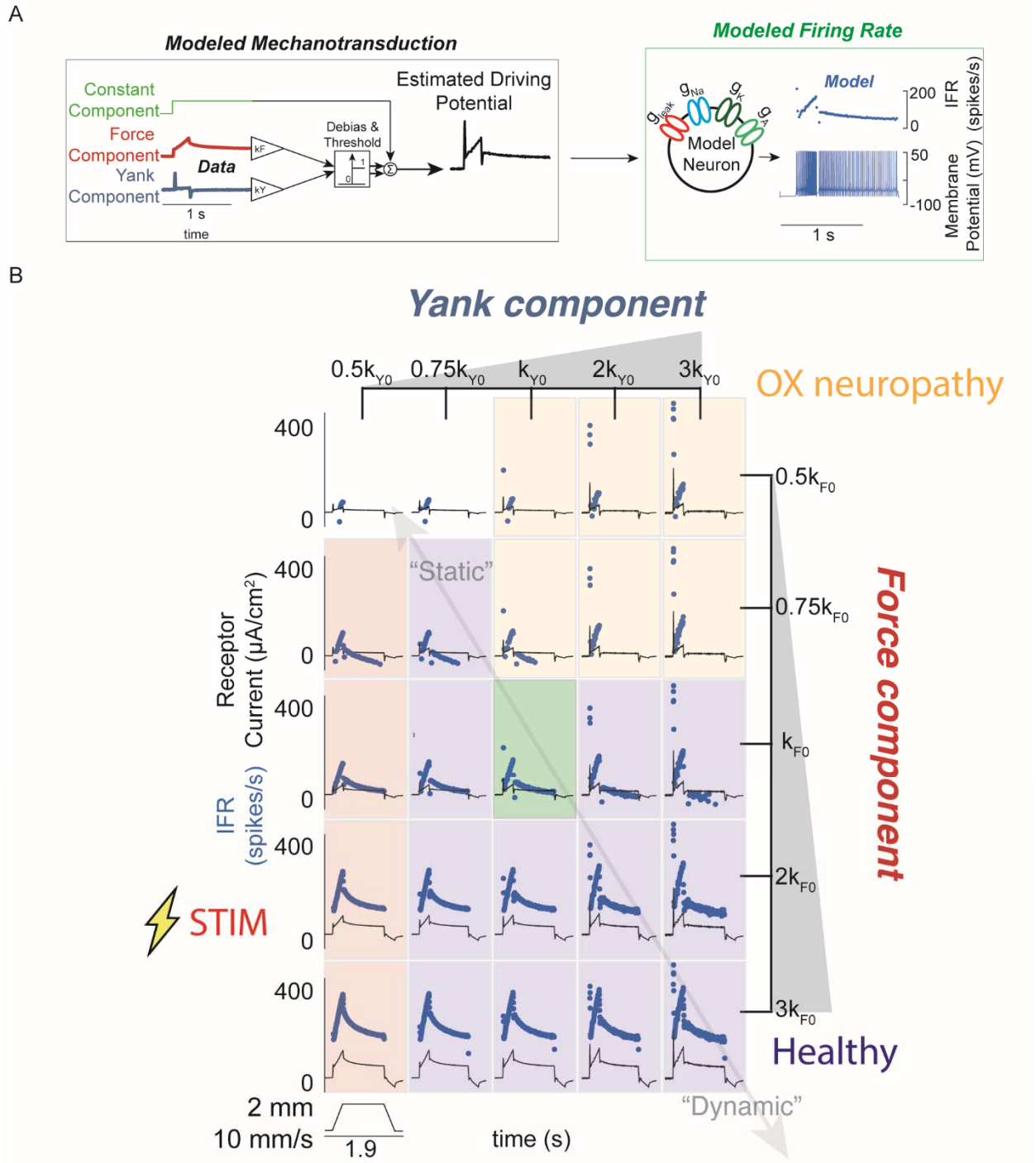

Figure 3 Spectrum of passive muscle spindle firing phenotypes accounted for by varying sensitivity to experimentally-derived muscle fiber force and yank. A) Sensitivity to experimentally-derived force and yank was systematically varied for a single stretch and resultant driving potentials were input to a Connor-Stevens model neuron to generate firing patterns. B) Nominal force and yank weights were identified to recreate experimentally-recorded muscle spindle response to a representative stretch (green box). Increasing sensitivity to yank (left to right) generated larger initial bursts and dynamic responses during the ramp, and resembled responses from oxaliplatin-treated specimens at the highest yank and lowest force

sensitivities (orange boxes, compare to Figure 2E). Increasing sensitivity to force (top to bottom) generated higher firing rates during the hold period and resembled Ia afferent firing responses after axonal stimulation at the lowest yank and highest force sensitivities (red boxes, compare to Figure 2F). Varying the weights of the force and yank sensitivities could recreate the spectrum of healthy muscle spindle firing profiles reported classically (purple boxes).

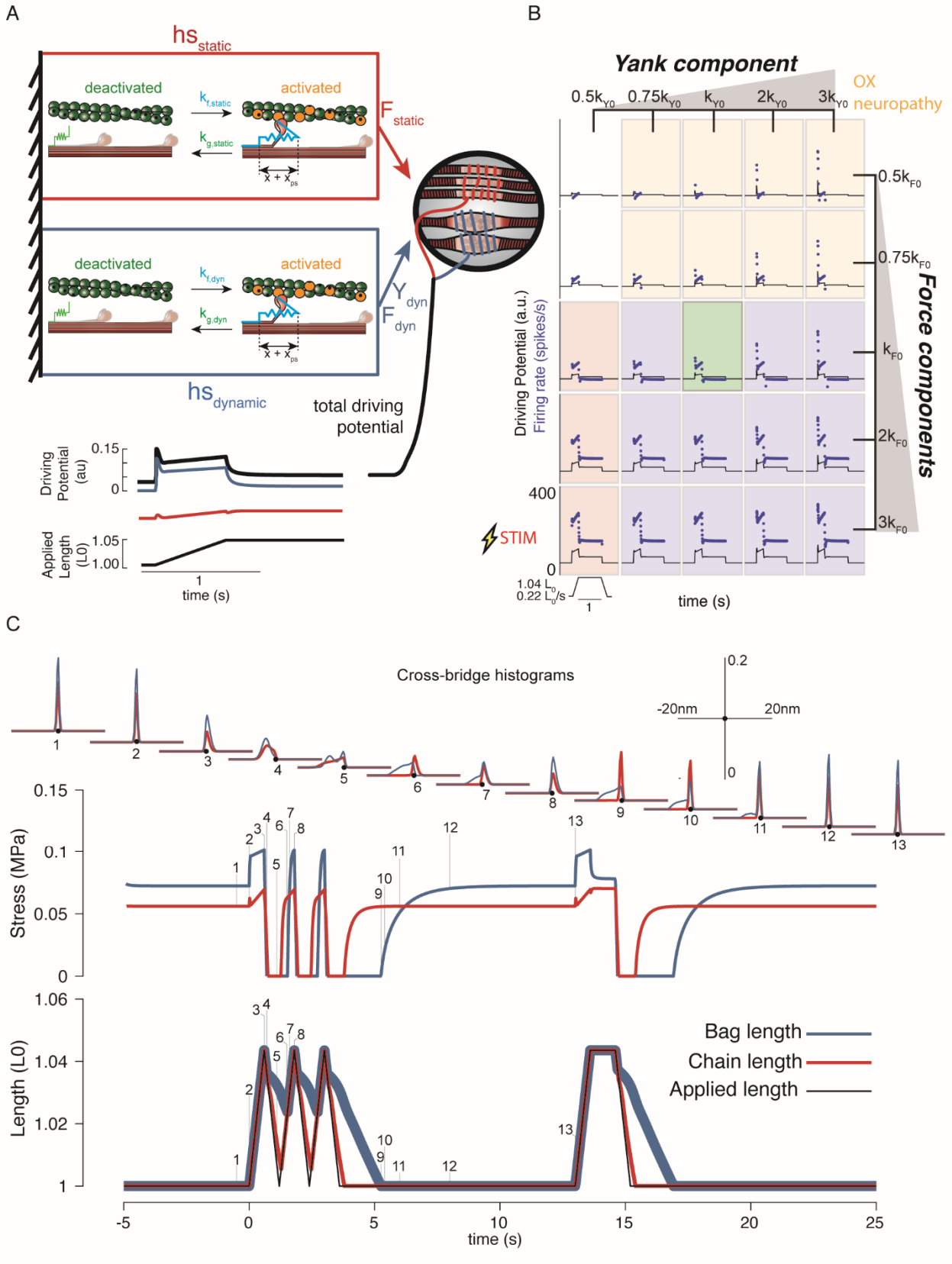

Figure 4 Generative model of muscle spindle driving potentials based on simulated muscle cross-bridge kinetics. A) The muscle spindle model consists of two muscle fibers in a parallel mechanical arrangement, loosely representing intrafusal bag and chain fibers. B) During stretch, force and yank of the "dynamic" fiber is linearly combined with force of the "static" fiber, with different proportions generating driving potentials consistent with "dynamic" and "static" muscle spindle firing response phenotypes. C) A population of myosin cross-bridges and their relative displacement and velocity with respect to active actin binding sites was simulated during three consecutive ramp-stretch-release stretches. The distribution of cross-bridge lengths relative to actin binding sites is shown at different timepoints of imposed kinematics (numbered graphs and timepoints). The length of the dynamic and static fibers (lower trace) and the stress in the dynamic and static fibers (middle trace) is shown. Deviations between applied length and muscle fiber length occur due to muscle fiber slack.

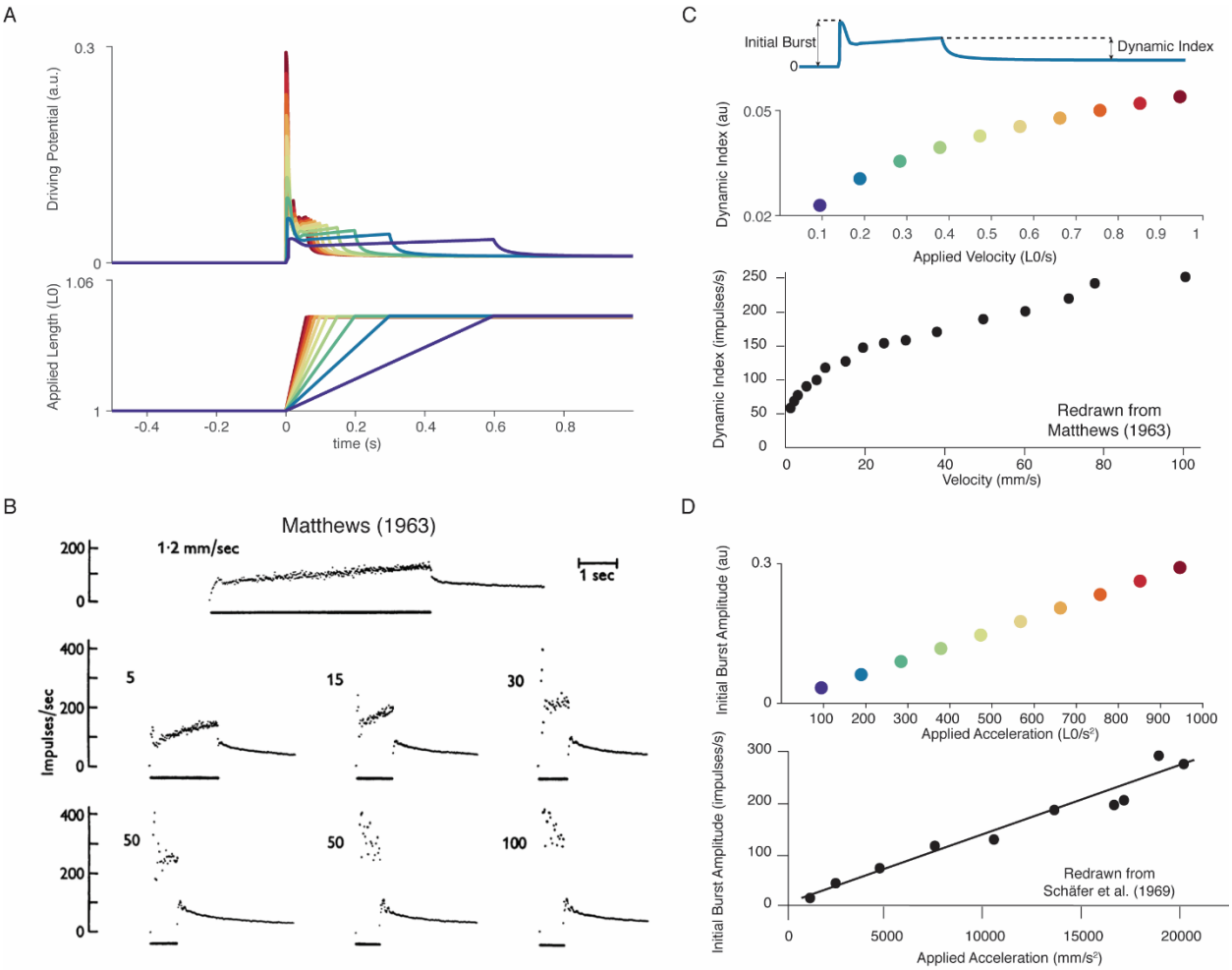

Figure 5 Muscle spindle firing dynamics emerge from cross-bridge mechanisms during simulated muscle stretch. Simulations assume a low level of muscle cross-bridge cycling consistent with relaxed muscle. Length displacements were imposed on the muscle fiber. A) Predicted driving potentials (upper traces) during ramp stretches of varying velocity and acceleration (lower traces). B) Classical data showing Ia afferent firing modulation with different stretch velocity (Matthews 1963). C) Dynamic index emergent from cross-bridge mechanisms. Dynamic index is defined classically as the ratio of firing rate at the end of the ramp phase and the firing rate 0.5 seconds into the hold phase (upper diagram). The muscle spindle model exhibits a sublinear relationship between dynamic index and stretch velocity (middle plot – colors correspond to A), similarly to classical findings (bottom plot). E) Linear acceleration scaling of initial burst emergent from cross-bridge mechanisms. Initial burst amplitude is defined as the difference between peak firing rate during initial burst and baseline. Muscle spindle model exhibits linear scaling with stretch acceleration at stretch onset (top plot), which is consistent with classical findings (bottom plot – Schäfer 1969). Figures reproduced from Matthews (1963) and Schäfer et al. (1969).

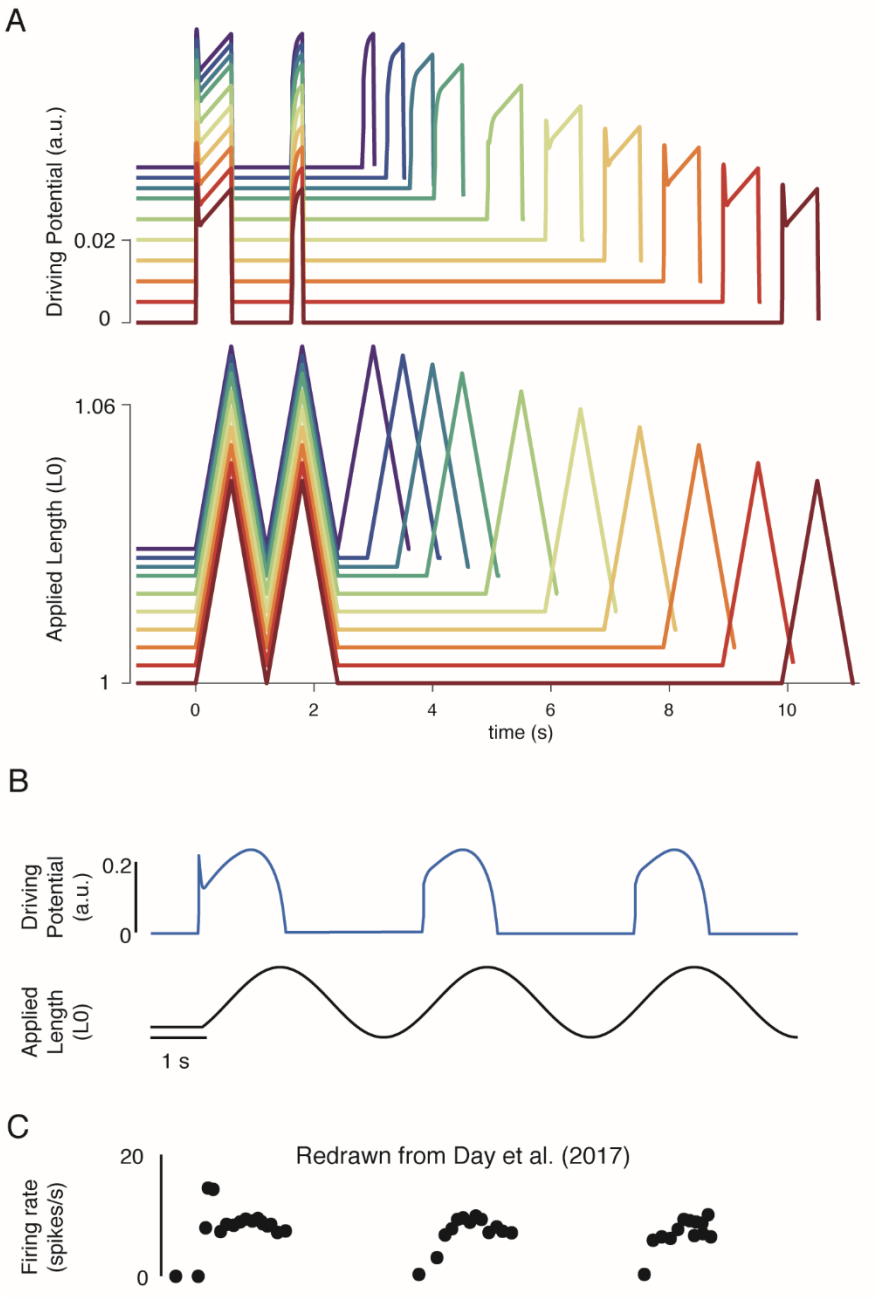

Figure 6 Emergent movement history-dependence of muscle spindle. A) When repeated stretch-shorten length cycles were applied, a larger response was predicted if the length was held constant prior to stretch (bottom plot – all traces). An abolished initial burst and reduced dynamic response were predicted in the second stretch, immediately applied after the length was returned to the initial value (top plot – all traces). In the third stretch, recovery of the initial burst was dependent on the time interval between the second and third stretch, with the effect saturating between 5-10 s (top plot, recovery from violet to red traces). This finding predicts the results found by Haftel et al. (2004) in rat muscle spindles. Similarly, dynamic response recovered gradually with time interval between second and third stretch (top plot, recovery from

violet to red traces). This finding predicts the results found by Proske and Stuart (1985) in toad muscle spindles. B) Sinusoidal displacement imposed from rest elicited a history-dependent initial burst in the predicted muscle spindle driving potential at the onset of stretch, resembling data from C) human muscle spindles recorded during the application of sinusoidal motion to the ankle in relaxed conditions (Day et al. 2017).

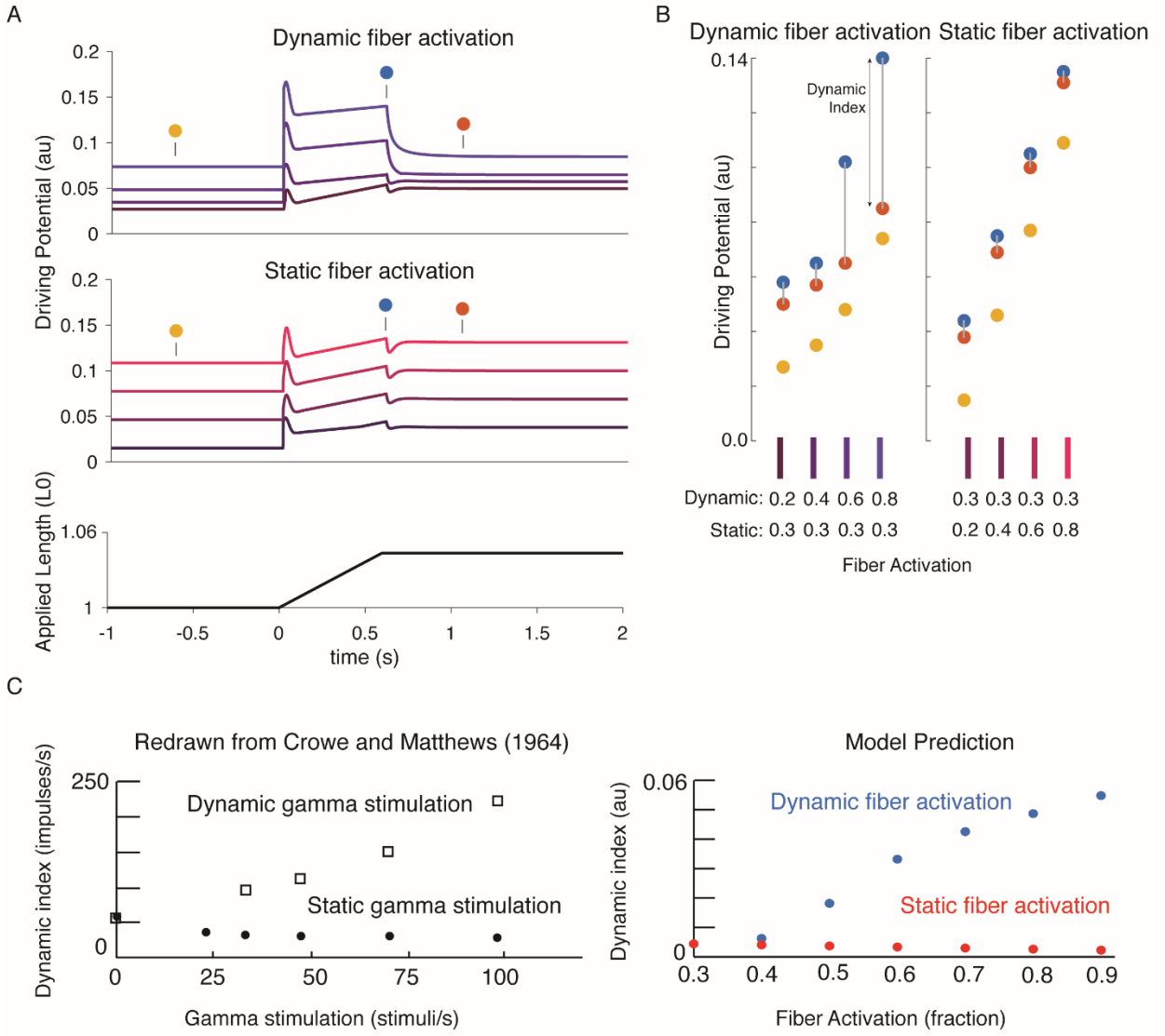

Figure 7 Changes in muscle spindle sensitivity caused by central drive emergent from interactions between dynamic and static fibers. Fusimotor activity was imposed on either the dynamic or the static fiber by increasing the number of active actin binding sites in the appropriate fiber. A) Simulated dynamic fiber activation increased the driving potential predominantly during the ramp, with smaller increases during the background and hold period (top traces). Simulated static fiber activation predominantly increases the driving potential rate during the background and hold period, with only modest increases in during the ramp. B) Emergent scaling of the dynamic index with dynamic (increase in dynamic index) and static fiber activation (decrease in dynamic index) resembled trends reported previously in the literature with C) dynamic index increasing with bag fiber activation, and dynamic index decreasing with chain fiber activation, respectively. Figures adapted and reproduced from Crowe and Matthews (1964) with permission.

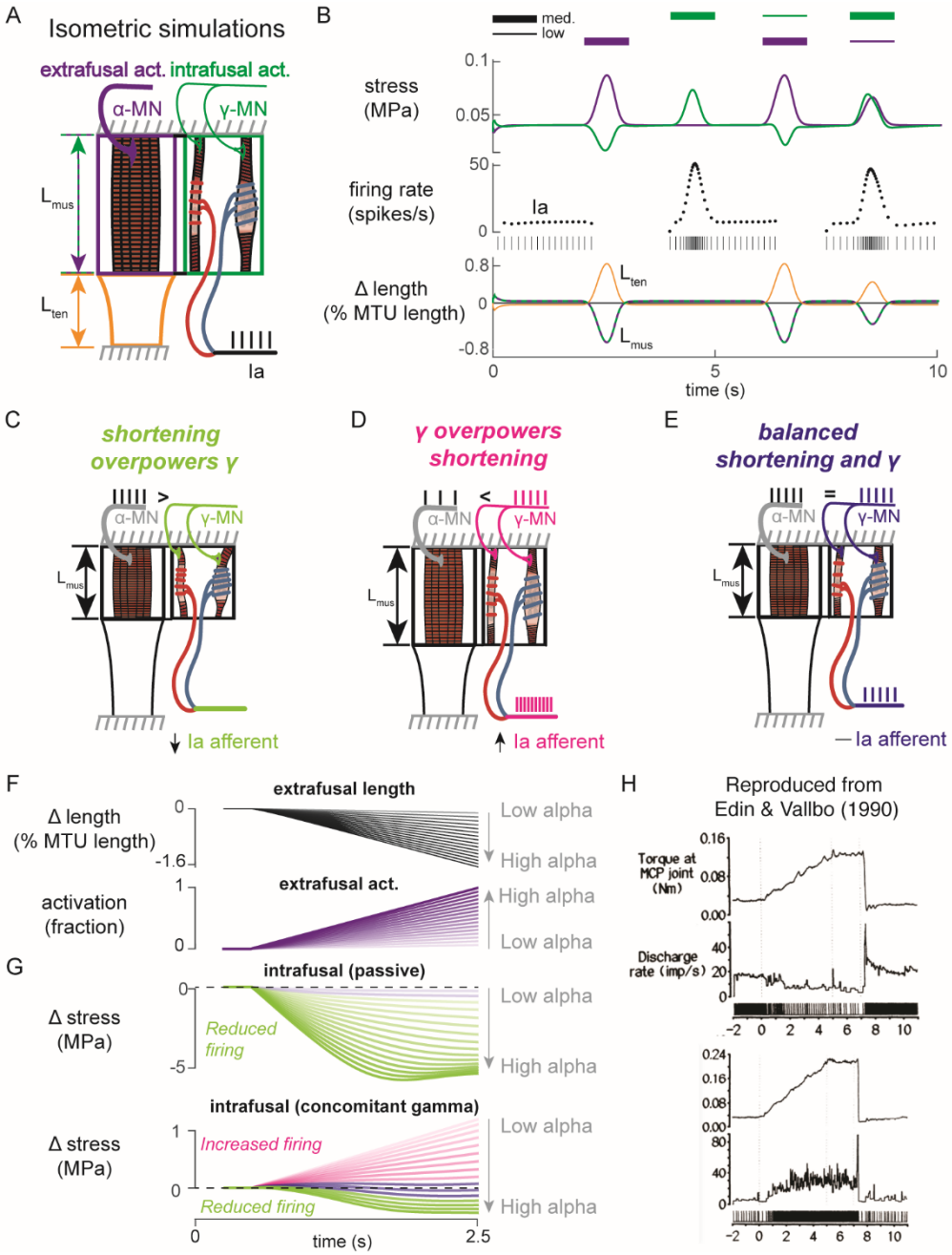

Figure 8

Paradoxical muscle spindle firing activity during isometric musculotendon conditions emergent from multiscale muscle mechanics. A) Framework of isometric musculotendon simulations. We simulated an in-series muscle-tendon with ends fixed to its initial length. The extrafusal muscle length was shared with the intrafusal muscle fibers, which were activated independently from the extrafusal muscle. B) Decoupling of intra- and extrafusal force during short isometric contractions. Different combinations of extrafusal (purple bars) and intrafusal (green bars) activation were simulated. Top row contains intra- (green) and extrafusal (purple) stress during these conditions. Middle row is the simulated Ia afferent firing rate, generated by using our mechanistic model simulated driving potential combined with a leaky integrate-and-fire neural

model. Extrafusal activation shortens the extrafusal muscle, and in the absence of sufficient intrafusal activation, silences the Ia afferent firing. Intrafusal activation by itself causes the Ia afferent to fire more. When both intra- and extrafusal muscle are activated concomitantly, the relative weighting of activity determines whether the Ia afferent will increase or decrease its firing rate. C-E) Schematic representation of the multi-scale mechanics responsible for Ia afferent behavior in these simulations. When the effects of extrafusal shortening overpower the effect of fusimotor activity on the spindle, the Ia afferent firing rate decreases, or stops altogether (left, green). When fusimotor activity overpowers the effect of extrafusal shortening on the spindle, the Ia afferent firing rate increases (center, pink)). In theory, this suggests there are combinations of fusimotor activity and shortening that will result in no net change to the Ia afferent firing, despite the dynamics of the muscle (right, blue). F) A spectrum of musculotendon isometric conditions arising from the interplay of extrafusal shortening and intrafusal activation. We activated the musculotendon model with ramp activations and simulated the intrafusal muscle force with and without concomitant gamma activation. When increasing alpha motor neuron drive (purple traces; directionally indicated in all plots by an arrow), extrafusal muscle shortened more (top plot). G) The passive spindle always decreased its force because of the shortening imposed by the surrounding extrafusal muscle (top plot). When the intrafusal muscle was activated with concomitant drive, similar to the largest amplitude ramp of extrafusal muscle, we observed the spectrum of responses predicted in C-E: the intrafusal force either decreased (green), stayed relatively constant (purple), or increased (pink). H) Experimental examples of one muscle spindle decreasing its firing rate (top traces) and another increasing its firing rate (bottom traces) during an isometric task in human. Figure reproduced from Edin and Vallbo (1990) with permission.

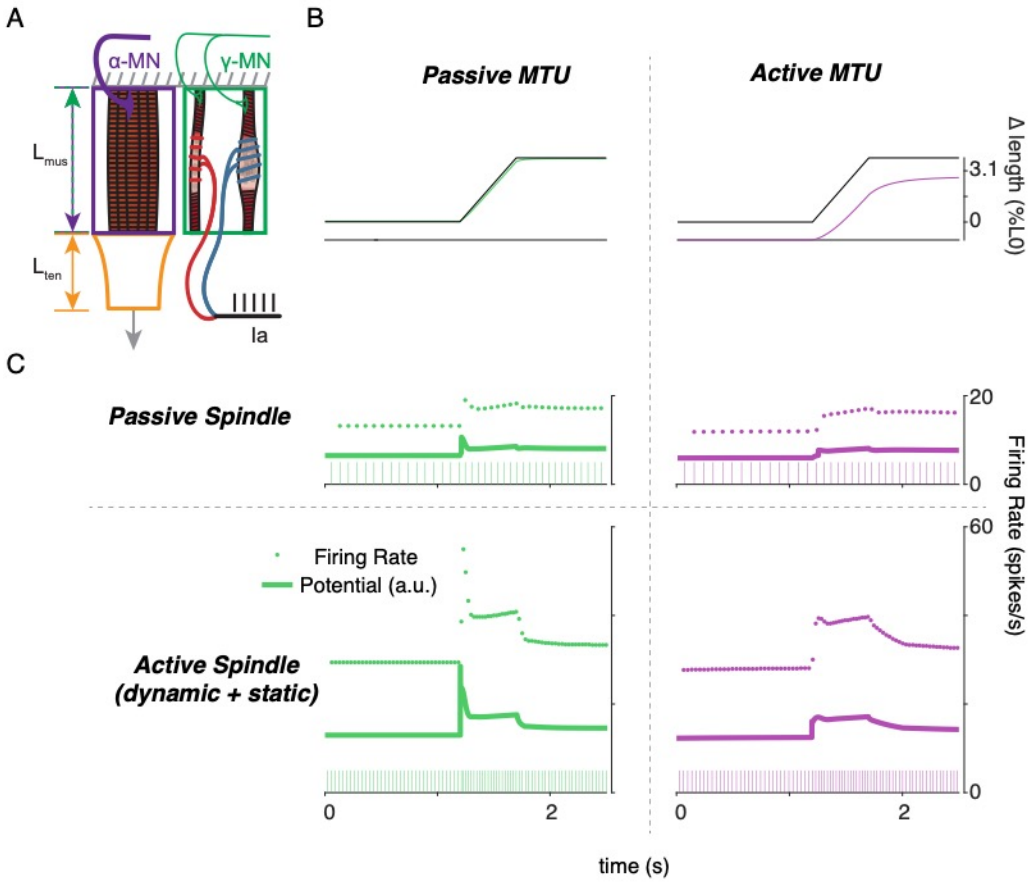

Figure 9

Complex interplay of movement, alpha, and fusimotor drive underlie muscle spindle Ia firing rates. A) Framework of free-end musculotendon simulations. We simulated an in-series muscle-tendon with one end fixed and one end free to move. The extrafusal muscle length was shared with the intrafusal muscle fibers, which were activated independently from the extrafusal muscle. B) Passive musculotendon has a relatively compliant muscle, leading to a MTU length change being primarily applied to the muscle, not the tendon. Extrafusal activation creates a relatively stiff muscle, leading to a smaller length change for the same MTU length applied. C) Musculotendon activation changes the coding properties of both passive and active muscle spindles. When the MTU is passive, a passive muscle spindle has an initial burst.

METHODS

Animal care

All procedures and experiments were approved by the Georgia Institute of Technology's Institutional Animal Care and Use Committee. Adult female Wistar rats (250–300 g) were studied in terminal experiments only and were not subject to any other experimental procedures. All animals were housed in clean cages and provided food and water ad libitum in a temperature- and light-controlled environment in Georgia Institute of Technology's Animal facility.

Terminal physiological experiments

Experiments were designed to measure the firing of individual muscle afferents in response to controlled muscle stretch using conventional electromechanical methods applied in vivo as reported by Vincent et al. 2017 (see Fig. 1). Briefly described, rats were deeply anesthetized (complete absence of withdrawal reflex) by inhalation of isoflurane, initially in an induction chamber (5% in 100% O_2) and maintained for the remainder of the experiment via a tracheal cannula (1.5–2.5% in 100% O_2). Respiratory and pulse rates, Pco_2, P_{O2}, blood pressure, and core temperature were maintained within physiological ranges variously by injecting lactated ringers subcutaneously and by adjusting anesthesia and radiant heat. Rats were secured in a rigid frame at the snout, lumbosacral vertebrae, and distally on the left femur and tibia (knee angle 120°). Dorsal roots S1-L4 were exposed by laminectomy and supported in continuity on a bipolar recording electrode. Triceps-surae muscles in the left hindlimb were dissected free of surrounding tissue and their tendon of insertion was cut and attached to the lever arm of a force and length-sensing servomotor (Model 305C-LR, Aurora Scientific Inc.). Triceps surae nerves were placed in continuity on monopolar stimulating electrodes, and all other nerves in the left hindlimb were crushed to eliminate their contribution to muscle-stretch evoked action potentials recorded in dorsal roots. Exposed tissues were covered in pools of warm mineral oil Surgical and recording preparation

539 followed by data collection (see below) lasted for up to 10 hrs. At the conclusion of data collection, rats
540 were killed by exsanguination preceded either by overdose with isoflurane inhalation (5%).

541 Data collection centered on trains of action potentials recorded from individual primary sensory
542 neurons responding to length perturbations of the parent triceps surae muscles. Action potentials were
543 recorded intracellularly from axons penetrated by glass micropipettes in dorsal root. Sensory axons were
544 identified as triceps surae when responding with orthodromic action potentials evoked by electrical
545 stimulation of the corresponding muscle nerves. Axons selected for further study were classified as group
546 Ia when (a) isometric twitch contractions interrupted muscle stretch-evoked firing, (b) each cycle of high
547 frequency (>200Hz), low amplitude (80μm) muscle vibration evoked action potentials, and (c) muscle
548 stretch produced an initial burst firing of high frequency (>100Hz) firing at the onset of rapid muscle
549 stretch.

550 Ia afferents were studied for their firing responses to two forms of muscle stretch beginning from
551 and returning to $L_{r(rest)}o$, which was the muscle length corresponding to 10 grams passive muscle force:
552 (1) ramp-hold-release stretch (20mm/s constant velocity ramp and release with intervening hold to 3 mm
553 length) repeated every 4 secs and (2) sequential triangular ramp-release stretches to 3 mm at constant
554 velocity (4 mm/s). Records of action potentials, muscle force and length were digitized and stored on
555 computer for later analysis.

556 In the 11 Ia afferents for which the initial pseudolinear model analyses were performed, a range
557 of 6-99 stretch trials with varying maximum length and velocity were achieved depending on the
558 recording stability. To ensure sufficient information for statistical measures, we required that stretch trials
559 have at least 50 recorded action potentials in order to be included in statistical analyses. Stretch trials
560 where spikes were not discriminable were excluded. These criteria yielded suitable datasets for 11
561 individual afferents from 5 animals for pseudolinear model analyses and 6 individual afferents from 5
562 animals for the axonal stimulation analyses. We also included 3 afferents from 3 rats treated with
563 oxaliplatin (Bullinger et al., 2011b).

564

565

566

567 *Muscle fiber force estimation*

568 To isolate the component of recorded musculotendon force arising from the muscle fibers (used
569 as a proxy for intrafusal muscle force), we assumed an idealized musculotendon mechanical arrangement
570 (Fig. 1). In summary, we assumed there was noncontractile passive connective tissue arranged
571 mechanically in parallel with the muscle fibers and removed it analytically, as previously described
572 (Blum et al., 2019).

573 Briefly, we assumed the noncontractile tissue acted as a nonlinear spring of the form:

574

$$F_{nc} = k_{lin}(L - L_0) + Ae^{k_{exp}(L-L_0)}$$

575 where k_{lin}, k_{exp}, and A are greater than or equal to zero. Once parameters were selected by the
576 optimization procedure, the estimated noncontractile tissue forces were subtracted from the recorded
577 force to estimate the muscle fiber force, which was fit to the IFRs.

578

579 *Pseudolinear models for predicting firing responses*

580 We predicted spiking responses using pseudolinear combinations of either recorded
581 musculotendon length-related (length, velocity, and acceleration) or force-related (estimated muscle fiber
582 force and yank) variables (Fig. S1). The relative weights and offsets for each variable in a model were
583 optimized to minimize the squared error between the model prediction and Ia spike rates on a per-trial
584 basis.

585 For both the force- and length-related models, we fit the estimated IFR for each model to the IFR
586 of the afferent for each stretch trial included in our analyses (for all 20 afferents presented in this study).
587 The model parameters, consisting of a weight (k_i) and offset (b_i) for each force- or length-related variable

included in the sum, were found via least-squares regression using MATLAB's optimization toolbox (*fmincon.m*) and custom scripts.

We observed a peak to peak delay from the whole musculotendon yank and the initial burst, likely caused by delayed force transmission to the intrafusal fibers from the tendon (Blum et al., 2019). A time delay (λ_j) was determined by shifting the timestamp of the variables forward relative to the IFR data to be fit (note: this time delay was 0 for all variables except yank, to account for the apparent delay between the onset of muscle force response and the onset of the spiking response). The general form of the models was:

$$IFR_{j,n}(t) = \left(\sum_{i=1}^{n} k_i \cdot \left(\lfloor x_i(t - \lambda_j) \rfloor + b_i \right) \right) \quad (1)$$

where the IFR estimate of the *j*th model for the nth perturbation was estimated by a sum of n force- or length-related variables, offset by a single value, b_i, and scaled by a gain, k_i. $\lfloor\ \rfloor$ denote positive values of the argument. Model estimates for IFR were related to the recorded IFR of the mth afferent by the equation:

$$IFR_{j,n}(t) + e(t) = IFR_{m,n}(t) \quad (2)$$

Error, $e(t)$, was minimized by finding the set of parameters for each model that minimizes a measure related to $e(t)^2$.

Antidromic Axonal stimulation dataset

To test whether the force and yank components could arise from separate mechanosensitive mechanisms, another set of experiments was performed on 6 additional afferents in 4 animals. Each dataset consisted of three ramp-hold-release stretches repeated at 4 sec intervals . The second of three stretches was preceded by antidromic action potentials in a 50 Hz train lasting 500 ms. These action potentials were isolated exclusively to the Ia afferent under study by injecting suprathreshold current

609 pulses (0.5ms) directly into the axon through the micropipette located in the dorsal root. The first and
610 third stretches were unconditioned and served as bookend controls

611 For each trial in these 6 afferents, we found the best-fit prediction for the force-related model
612 using the parameter optimization described earlier. For the pre- and post-stimulation control trials, we
613 first fit the model without a yank component, and then refit the model with a yank component. For the
614 trials in which the electrical stimulus was applied, the yank component was set to be zero and the force
615 and constant components were optimized as described before.

616 We performed one-way ANOVA on model performance (R^2), yank sensitivity (k_Y), force
617 sensitivity (k_F), and the constant component (C) across 5 groups of model fits: pre-stimulus control trials
618 without (1) and with (2) yank sensitivity, stimulus trials (3), and post-stimulus trials without (4) and with
619 (5) yank sensitivity. We used the Tukey-Kramer method to examine all pairwise comparisons between
620 groups.

621

622 *Oxaliplatin dataset*

623 We used data collected previously to test whether force and yank components were altered by
624 oxaliplatin chemotherapy alone (Bullinger et al., 2011b). The effect of oxaliplatin on sensory coding of
625 Ia afferents has been well-documented, so we analyzed three afferents from different animals. We fit the
626 muscle fiber force-related model (described above) to three stretch trials for each afferent (3mm, 20
627 mm/s). We performed one-way ANOVA on model performance (R^2) between model fits with and without
628 yank for each afferent to test the significance of the yank component on model performance.

629

630 *Applying estimated fiber force-related driving potentials to model neuron*

631 To test the feasibility of the force, yank, and constant components of the muscle fiber force-
632 related model as mechanical signals encoded by the muscle spindle receptor, we applied a range of
633 combinations of components to a conductance-based model neuron (based on the Connor-Stevens model;
634 see next section) and examined the resulting firing rates. We first estimated the muscle fiber force and

yank, as described previously, and varied the relative gains of these signals before adding them with a constant component. Once the components were added together, they were half-wave rectified, and applied to the model neuron as a stimulus current.

Model neuron sensitivities to these components were tuned until the model instantaneous firing rate was within 10 spikes/s for initial burst, dynamic response, and final plateau. We treated the parameter values which produced this response as the nominal values for the model. The relative sensitivities of the model neuron to force and yank component were then swept from 10-600% of their respective nominal values. We then compared the resulting changes in predicted firing rates with different phenotypical muscle spindle responses observed from these and other experiments.

Responses of muscle spindle Ia afferents to stretch

Consistent with prior studies, all Ia afferents exhibited initial bursts at onset of applied stretch, followed by a dynamic response during constant velocity stretch, and a period of rate adaptation during the subsequent isometric hold period. When repeated ramp-release length-changes were applied to the muscle, an initial burst and dynamic response was present during the first ramp, but the initial burst was absent and dynamic response was reduced during subsequent stretches–a phenomenon in Ia afferents known as history-dependence (cf. Haftel et al. 2004).

The population of 11 Ia afferents considered for the first analysis varied in sensitivity to stretch length, velocity, and acceleration. More dynamic afferents, as quantified by dynamic index (P. B. C. Matthews, 1963a) typically had relatively large spike responses during positive velocity stretch. More static afferents exhibited more firing during the plateau phase of stretch, with relatively smaller dynamic indices. The population of afferents also exhibited a range of initial burst amplitudes in response to stretch. There was no clear relationship between the dynamic index and initial burst amplitudes for a given afferent. Despite the differences in sensitivity amongst the afferent population, the waveforms of

afferent responses to the same stretch stimuli contained the same features (i.e. all afferents exhibited initial bursts, dynamic responses, and rate adaptation to varying degrees).

Conductance-based model neuron for reproducing spiking activity

To demonstrate the plausibility of force- and yank-related ionic currents caused by stretch, we used a modified Connor-Stevens conductance-based model neuron to model the transformation of graded receptor potentials into action potentials by the afferent (Connor & Stevens, 1971). The model neuron contained a fast sodium, delayed rectifier potassium, transient potassium, and leak conductances implemented in Simulink using built-in differential equation solvers (ode23s.m).

Intrafusal muscle model

All intrafusal muscle model code and scripts used to generate the data presented in this study are available at https://github.com/kylepblum/MechanisticSpindleManuscript.git. If interested in using the model as implemented in this study, a description of how to use it is also available there.

To simulate the hypothesized history-dependent mechanisms of intrafusal muscle fibers, we used a computational model of cross-bridge cycling. We implemented a model in MATLAB based on a simplified structure of the model developed by Campbell (K. S. Campbell & Lakie, 1998; K. S. Campbell & Moss, 2000; Kenneth S. Campbell, 2014b; Kenneth S. Campbell & Moss, 2002) (Supplemental Fig. 5). Instead of simulating the coupled dynamics between myosin heads and actin binding sites (Kenneth S. Campbell, 2014b), we focused on the thick filament kinetics and greatly simplified the thin filament. In brief, the force in each half sarcomere was calculated as a sum of two components: an active component generated by the cycling activity of a population of myosin heads and a passive component generated by a simulated linear spring modelling the contributions of titin in the half sarcomere:

$$Total\ Force = \int_{-\infty}^{+\infty} \left(k_{cb}\ \rho f(x)\left(x + x_{ps}\right) dx\right) + k_{pas}(l_{hs} - l_0)$$

683

684 The model calculates the force of a half sarcomere at each time step by adding the forces generated from
685 each myosin head attached to an actin binding site (active force) with the elastic force of titin (passive
686 force). The active force is calculated as the fraction of attached myosin heads, f, multiplied by the
687 number density, ρ, unit stiffness of a single attached actin-myosin cross-bridge, k_{cb}, multiplied by the
688 length of the cross-bridges, $x + x_{ps}$ (where x_{ps} represents the additional displacement of an attached
689 cross-bridge required to generate a "powerstroke" force when multiplied by k_{cb}), integrated across cross-
690 bridge lengths. The passive force is calculated as the length of the half sarcomere, l_{hs}, relative to a
691 reference length, l_0, multiplied by a linear stiffness, k_{pas}.

692 To simplify the coupled dynamics of Campbell, we decided to control intrafusal activation
693 directly instead of ionic calcium concentration:

$$\frac{df_{act}(t)}{dt} = u(t),$$

694 Where the change in the fraction of activated actin binding sites, $df_{act}(t)$, is determined by user input
695 u(t).

696 The myosin cycling dynamics were modelled using a two-state system in which each myosin
697 head could either be attached as a cross-bridge with length x, or detached. The numbers of myosin heads
698 in each of these states were governed by the system of partial differential equations, as in Myosim:

$$\frac{\delta A(x,t)}{\delta t} = k_f(x)D(t) - k_g(x)A(x,t)$$

$$\frac{\delta D(t)}{\delta t} = \int_{-\infty}^{+\infty} k_g(x)A(x,t)dx - \int_{-\infty}^{+\infty} k_f(x)D(t)dx$$

699 where $A(x,t)$ is the number of attached myosin heads attached to actin binding sites at time t extended by
700 length x and $D(t)$ is the number of myosin heads in the detached state. The rate equations $k_f(x)$ and

$k_g(x)$ are the forward and reverse rates of myosin attachment, respectively, and are both functions of cross-bridge length, x. The partial differential equations were simplified into a system of ODEs by solving the time-dependent equations simultaneously at each cross-bridge length. The resulting system of ODEs was solved using a built-in Matlab ODE solver (*ode23*.m). Thick filament dynamics are coupled to the activation of the thin filament by the number of cross-bridges participating in cycling:

$$n(t) = \int_{-\infty}^{+\infty} A(x,t)dx + D(t)$$

where the fraction of bound cross-bridges is defined by the thick filament:

$$f_{bound}(t) = \int_{-\infty}^{+\infty} A(x,t)dx,$$

and the number of detached cross-bridges is defined by the thin filament activation and $f_{bound}(t)$:

$$D(t) = f_{act}(t) - f_{bound}(t).$$

There are two modes of operation for these muscle models: length control model and slack mode. The model switches between the two modes automatically, based on whether each intrafusal fiber is taut (force greater than zero) or slack (force equal to zero).

Length control mode is used by the model when the half sarcomere length is equal to the end-to-end length of the sarcomere (i.e., the half sarcomere is not slack). When in length control mode, the command length is applied directly to the half sarcomere, and the system of differential equations is solved as described earlier. The half sarcomere is updated in the following order: 1) The length of the half sarcomere and calcium concentration are each updated by the change in command length and change in command calcium concentration applied to the model, respectively, 2) the amount of filament overlap is updated, 3) thin filament dynamics are updated, 4) the population of myosin heads are allowed to evolve, and 5) the population of myosin heads is moved according to the change in length of the half sarcomere.

719 Slack mode contains several extra steps for solving the equations governing the model. At every
720 time step, the model uses an iterative search (*fzero.m*) to find the length at which the force in the current-
721 state half sarcomere would reach zero and compare it to the command length. If the command length is
722 smaller than the "slack length" calculated, the model enters into slack mode; otherwise, the model stays in
723 length control mode.
724 Once the model enters into slack mode, the model first evolves the cross-bridge distribution in
725 time based on the system of differential equations described earlier. The model then repeats the iterative
726 search to find the slack length for the half sarcomere given the new cross-bridge distribution and shifts it
727 to the slack length for the half sarcomere. At the next time step, the model repeats the comparison
728 between the command length and the slack length for the current state of the half sarcomere. If the
729 command length is greater than the slack length, the model returns to length control mode; otherwise, the
730 model stays in slack mode.
731
732 *Intrafusal muscle model parameters*
733 Model parameters were either chosen to match the default parameters from Campbell (Kenneth S.
734 Campbell, 2014a), so the model would exhibit history-dependence at the time-course measured in this
735 work, or based on the limited qualitative information we have regarding intrafusal muscle fibers (Thornell
736 et al., 2015b). All simulations used the same set of model parameters (Supplemental Table S1).
737 Myosin attachment and detachment rates equations, $k_f(x)$ and $k_g(x)$, were selected such that the
738 force response of the model would exhibit history-dependent features consistent with observations in both
739 permeabilized muscle fibers and instantaneous firing rates of muscle spindle Ia afferents. The bag and
740 chain fibers were differentiated by relatively slower myosin attachment kinetics in the bag fiber and a
741 more compliant passive elastic element (M H Gladden & Boyd, 1985; Margaret H. Gladden, 1976;
742 Thornell et al., 2015a). Proske (U. Proske et al., 1992; Uwe Proske et al., 2014; Uwe Proske & Gandevia,
743 2012) hypothesized that history-dependent muscle spindle IFRs (and corresponding perceptual errors) are

744 caused by a population of cross-bridges within the intrafusal muscle that are unable to "keep up" with the
745 rate of shortening during an imposed movement, causing the intrafusal muscle fibers to fall slack. To
746 model this behavior, we selected rate equations that would produce relatively slow cross-bridge
747 reattachment during shortening, but would retain other desired characteristics, such as short-range
748 stiffness.
749

750 *Model of muscle spindle responses to stretch of intrafusal muscle*

751 To model the transformation of intrafusal muscle fiber stress into a firing waveform, we used a
752 pseudolinear combination of force and its first time-derivative, yank, based on previously published
753 observations (Blum et al., 2017). Our model consists of two intrafusal muscle fiber models, a "static"
754 fiber and a "dynamic" fiber based on observations that muscle spindle primary afferent responses to
755 stretch consist of two components (Banks et al., 1997; Blum et al., 2017; Boyd, 1976; Boyd et al., 1977;
756 Hasan, 1983; Jami et al., 1982; Jami & Petit, 1979; Lewis & Proske, 1972). For these simulations, each
757 muscle fiber model used identical parameters, but the contribution of each fiber to the neural firing rate
758 varied. The equation describing the contribution of each fiber to the total firing rate is:

$$r(t) = r_{dynamic}(t) + r_{static}(t), \quad (15)$$

759 where the total firing rate of the afferent, $r(t)$, is a sum of the dynamic and static fiber components, or
760 $r_{dynamic}(t)$ and $r_{static}(t)$, respectively. The static component was defined as:

$$r_{static}(t) = k_{Fs}\, F_s(t), \quad (16)$$

761 where k_{Fs} is a constant and $F_s(t)$ is the total force in the static fiber. The dynamic component was defined
762 as:

$$r_{dynamic}(t) = \left[k_{Fd}\, F_d(t) + k_{\dot{F}d}\, \dot{F}_d(t)\right], \quad (17)$$

where k_{Fd} and $k_{\dot{F}d}$ are constants, and $F_d(t)$ and $\dot{F}_d(t)$ are respectively the force and yank of the cycling cross-bridges in the dynamic fiber. We used default k_{FS}, k_{Fd}, and $k_{\dot{F}d}$ values of 1, 1, and 0.03, respectively, unless otherwise noted.

The static and dynamic fibers are arranged in perfect mechanical parallel and were allowed to be activated independently. Thus, the actions of the dynamic and static fibers could be simulated simultaneously or sequentially.

Occlusion between dynamic and static components

To account for the evidence of so-called "occlusive interaction" between dynamic and static branches of the muscle spindle Ia afferent ending, we used a nonlinear summation of the static and dynamic components. Previous models have used complete occlusion (Hulliger et al., 1977; C.-C. K. Lin & Crago, 2002) but we used a partial occlusion based on more recent findings (Banks et al., 1997). With occlusion, the total firing rate of the model Ia afferent becomes:

$$r(t) = f_{occ} r_{dynamic}(t) + r_{static}(t), \qquad r_{dynamic} \geq r_{static} \tag{18}$$

$$r(t) = r_{dynamic}(t) + f_{occ} r_{static}(t), \qquad r_{static} > r_{dynamic} \tag{19}$$

where f_{occ} is an occlusion factor limiting the contribution of either component to the overall firing rate. This parameter was set to 0.3 (unitless) for all simulations unless otherwise noted (Banks et al., 1997).

Dynamic response simulations

To demonstrate the ability of our model to produce the classical fractional power relationship between the dynamic response of muscle spindle Ia firing rates and ramp velocity (Hasan, 1983; Houk et al., 1981; P. B. C. Matthews, 1963b), we applied a series of ramp-hold stretches to the model with each fiber's proportion of available binding sites set to 0.3 (Fig. 6A). The ramp stretches consisted of a pre-stretch isometric hold period, followed by a constant velocity stretch that varied linearly between trials from $0.079L_0$/s to $0.79L_0$/s, and another isometric hold period at its new length ($1.059L_0$). The duration of

784 stretch was shortened proportionally to the stretch velocity to ensure the same total length was applied in
785 each trial.

786 *Time-history dependence simulations*

787 To demonstrate the unique ability of our model to vary its own sensitivity to stretch based on the
788 history of movement applied to the muscle (Haftel et al., 2004), we applied series of triangular ramp-
789 release stretches with each fiber's activation set to 0.3. Each series consisted of three stretch-shorten
790 cycles, with a 1.047L_0 amplitude and stretch and shorten velocities of 0.079L_0/s. The first two cycles were
791 applied sequentially with no pause between them, whereas the third sequence was applied after a varied
792 isometric hold period at L_0 ranging from 0 – 10 s.

793 To demonstrate the robustness of our mechanistic model to produce history dependent responses
794 similar to those observed in awake humans, we approximated stimuli from microneurography studies in
795 humans from the lower limb (Day et al., 2017). We applied a 1.042 L_0 sinusoidal length change at 1.57
796 Hz to the model at the baseline activation to mimic the passive manipulation of the ankle in the study
797 (Day et al., 2017). To roughly match the predicted driving potential to the firing rate of the spindle, we
798 used k_{Fs}, k_{Fd}, and $k_{\dot{F}d}$ values of 1.8, 2, and 0.15, respectively.
799

800 *Tonic gamma activation simulations*

801 To demonstrate the effects of muscle activation on the firing response of our model (Fig. 7), we
802 applied a range of activations to the static and dynamic fibers (Emonet-Dénand et al., 1977). We varied
803 the activation levels of the static and dynamic fibers independently, between 0 – 1.0, before applying a
804 1.047L_0 ramp-hold stretch at a constant velocity of 0.079L_0/s. We used k_{Fs}, k_{Fd}, and $k_{\dot{F}d}$ values of 1.5,
805 0.8, and 0.03, respectively, for these simulations in order to better visualize the effects of gamma
806 activation on the predicted driving potential.

807 *Musculotendon stimulations*

To more completely address the complex interplay between alpha and fusimotor drive and the effect therein on the afferent outputs of the spindle, we created a model of a musculotendinous unit, comprised of a single half-sarcomere model mechanically in series with a linear elastic element to model the tendon. To balance the forces between the muscle and tendon, a force balancing operation was performed by searching iteratively for the pair of muscle and tendon length changes that would result in equal tendon and muscle forces.

To demonstrate the independent effects of alpha and fusimotor drive on the muscle spindle Ia afferent, we modeled a series of isometric activation pulses. Each pulse was based on a Gaussian waveform (*gausswin.m*) 1 second long, with a width factor of 0.3. Medium activation was defined as 50% peak activation, and low activation was defined as 25% peak activation for both extra- and intrafusal muscle. We simulated the musculotendon responses to these pulses and used the extrafusal muscle length as the length input to the intrafusal muscle fibers. We calculated the resulting firing rate using the previously defined *r*, from the force and yank of intrafusal models. As a visual aide, we generated a possible Ia afferent spike response by driving a leaky integrate-and-fire neural model with *r* as the input.

Next, we wanted to demonstrate the opposing effects of extrafusal muscle shortening and increasing fusimotor drive to mimic the effects of putative alpha-gamma coactivation during isometric conditions. To accomplish this, we emulated the microneurography work of Edin and Vallbo (Edin & Vallbo, 1990) by applying ramp increases to extrafusal activation with concomitant fusimotor ramps. We ran 16 simulations with increasing 2 second activation ramps with peak activation at the end of the ramp ranging from 25-100% extrafusal activation in linear increments. The intrafusal peak activation was 100% for all 16 simulations.

Finally, to demonstrate the combined interactions of alpha and fusimotor drive with musculotendon movements, we ran a set of simulations varying levels of extra- and intrafusal activation during an imposed stretch of the musculotendon. For each simulation, we applied a 3.8% L_0, 7.7% L_0/s ramp-hold stretch to the musculotendon under low (10%) and medium (60%) tonic extrafusal activation. For each of these conditions, we also simulated low (30%) and high (70%) tonic dynamic and static

834 intrafusal activation to highlight the effects of extrafusal activation on Ia afferent coding. As with the
835 isometric pulse simulations, we visualized Ia afferent spiking using a leaky integrate-and-fire neuron.
836
837 *Adaptation of previously published figures*
838 Previously published results that were used for comparison with our model predictions were
839 redrawn in Adobe Illustrator. Only single data points and lines were approximated by tracing over their
840 apparent geometric centroids. These data were redrawn for aesthetic purposes only and were not used for
841 any quantitative comparisons. Any comparison of data from these studies with the present study were
842 performed using the original manuscripts.

REFERENCES

A Schaafsma, E. O., & Willigen, J. D. V. (2002). A muscle spindle model for primary afferent firing based on a simulation of intrafusal mechanical events. *Journal of Neurophysiology*, 1–16.

Banks, R. W. (2005). *The muscle spindle*. http://scholar.google.comjavascript:void(0)

Banks, R. W. (2015). The innervation of the muscle spindle: A personal history. *Journal of Anatomy*, *227*(2), 115–135. https://doi.org/10.1111/joa.12297

Banks, R. W., Hulliger, M., Scheepstra, K. A., & Otten, E. (1997). Pacemaker activity in a sensory ending with multiple encoding sites: The cat muscle spindle primary ending. *Journal of Physiology*, *498 (Pt 1)*, 177–199. https://doi.org/10.1111/(ISSN)1469-7793

Bewick, G. S., & Banks, R. W. (2015). Mechanotransduction in the muscle spindle. *Pflugers Archiv: European Journal of Physiology*, *467*(1), 175–190. https://doi.org/10.1007/s00424-014-1536-9

Blum, K. P., Lamotte D'Incamps, B., Zytnicki, D., & Ting, L. H. (2017). Force encoding in muscle spindles during stretch of passive muscle. *PLoS Computational Biology*, *13*(9). https://doi.org/10.1371/journal.pcbi.1005767

Blum, K. P., Nardelli, P., Cope, T. C., & Ting, L. H. (2019). Elastic tissue forces mask muscle fiber forces underlying muscle spindle Ia afferent firing rates in stretch of relaxed rat muscle. *The Journal of Experimental Biology*, *222*(Pt 15). https://doi.org/10.1242/jeb.196287

Boyd, I. A. (1962). The structure and innervation of the nuclear bag muscle fibre system and the nuclear chain muscle fibre system in mammalian muscle spindles. *Philosophical Transactions of the Royal Society of London. Series B, Biological Sciences*, *245*(720), 92.

Boyd, I. A. (1976). The response of fast and slow nuclear bag fibres and nuclear chain fibres in isolated cat muscle spindles to fusimotor stimulation, and the effect of intrafusal contraction on the sensory endings. *Quarterly Journal of Experimental Physiology and Cognate Medical Sciences*, *61*(3), 203–254.

Boyd, I. A., Gladden, M. H., McWilliam, P. N., & Ward, J. (1977). Control of dynamic and static nuclear bag fibres and nuclearbag fibres and nuclear chain fibres by gamma and beta axons in isolated cat muscle spindles. *Journal of Physiology*. http://agris.fao.org/agris-search/search.do?recordID=US201302517703

Bullinger, K. L., Nardelli, P., Wang, Q., Rich, M. M., & Cope, T. C. (2011a). Oxaliplatin neurotoxicity of sensory transduction in rat proprioceptors. *Journal of Neurophysiology*, *106*(2), 704–709. https://doi.org/10.1152/jn.00083.2011

Bullinger, K. L., Nardelli, P., Wang, Q., Rich, M. M., & Cope, T. C. (2011b). Oxaliplatin neurotoxicity of sensory transduction in rat proprioceptors. *Journal of Neurophysiology*, *106*(2), 704–709. https://doi.org/10.1152/jn.00083.2011

Campbell, K. S., & Lakie, M. (1998). A cross-bridge mechanism can explain the thixotropic short-range elastic component of relaxed frog skeletal muscle. *The Journal of Physiology*, *510 (Pt 3)*, 941–962. https://doi.org/10.1111/j.1469-7793.1998.941bj.x

Campbell, K. S., & Moss, R. L. (2000). A thixotropic effect in contracting rabbit psoas muscle: Prior movement reduces the initial tension response to stretch. *The Journal of Physiology*, *525 Pt 2*(2), 531–548. https://doi.org/10.1111/j.1469-7793.2000.00531.x

Campbell, Kenneth S. (2014a). Dynamic coupling of regulated binding sites and cycling myosin heads in striated muscle. *The Journal of General Physiology*, *143*(3), 387–399. https://doi.org/10.1085/jgp.201311078

Campbell, Kenneth S. (2014b). Dynamic coupling of regulated binding sites and cycling myosin heads in striated muscle. *The Journal of General Physiology*, *143*(3), 387–399. https://doi.org/10.1085/jgp.201311078

Campbell, Kenneth S. (2016). Compliance Accelerates Relaxation in Muscle by Allowing Myosin Heads to Move Relative to Actin. *Biophysical Journal*, *110*(3), 661–668. https://doi.org/10.1016/j.bpj.2015.12.024

Campbell, Kenneth S. (2017). Super□relaxation helps muscles work more efficiently. *The Journal of Physiology*, *595*(4), 1007–1008. https://doi.org/10.1113/JP273629

Campbell, Kenneth S., & Moss, R. L. (2002). History-dependent mechanical properties of permeabilized rat soleus muscle fibers. *Biophysical Journal*, *82*(2), 929–943. https://doi.org/10.1016/S0006-3495(02)75454-4

Carrasco, D. I., Vincent, J. A., & Cope, T. C. (2017). Distribution of TTX-sensitive voltage-gated sodium channels in primary sensory endings of mammalian muscle spindles. *Journal of Neurophysiology*, *117*(4), 1690–1701. https://doi.org/10.1152/jn.00889.2016

Connor, J. A., & Stevens, C. F. (1971). Prediction of repetitive firing behaviour from voltage clamp data on an isolated neurone soma. *The Journal of Physiology*, *213*(1), 31–53. https://doi.org/10.1113/jphysiol.1971.sp009366

Cope, T. C., Vincent, J. A., Wieczerzak, K. B., Nardelli, P., & Rich, M. (2014). *Channelopathy contributes to proprioceptive deficits following chemotherapy*. Society for Neuroscience.

Crowe, A., & Matthews, P. B. (1964a). FURTHER STUDIES OF STATIC AND DYNAMIC FUSIMOTOR FIBRES. *The Journal of Physiology*, *174*, 132–151. https://doi.org/10.1113/jphysiol.1964.sp007477

Crowe, A., & Matthews, P. B. C. (1964b). The effects of stimulation of static and dynamic fusimotor fibres on the response to stretching of the primary endings of muscle spindles. *The Journal of Physiology*, *174*(1), 109–131. https://doi.org/10.1113/jphysiol.1964.sp007476

Day, J., Bent, L. R., Birznieks, I., Macefield, V. G., & Cresswell, A. G. (2017). Muscle spindles in human tibialis anterior encode muscle fascicle length changes. *Journal of Neurophysiology*, *117*(4), 1489–1498. https://doi.org/10.1152/jn.00374.2016

Dimitriou, M. (2014). Human muscle spindle sensitivity reflects the balance of activity between antagonistic muscles. *The Journal of Neuroscience*, *34*(41), 13644–13655. https://doi.org/10.1523/JNEUROSCI.2611-14.2014

Edin, B. B., & Vallbo, A. B. (1990). Muscle afferent responses to isometric contractions and relaxations in humans. *Journal of Neurophysiology*, *63*(6), 1307–1313. https://doi.org/10.1152/jn.1990.63.6.1307

Elek, J., Prochazka, A., Hulliger, M., & Vincent, S. (1990). In-series compliance of gastrocnemius muscle in cat step cycle: Do spindles signal origin-to-insertion length? *The Journal of Physiology*, *429*, 237–258. https://doi.org/10.1113/jphysiol.1990.sp018254

Ellaway, P. H., Taylor, A., & Durbaba, R. (2015). Muscle spindle and fusimotor activity in locomotion. *Journal of Anatomy*, *227*(2), 157–166.

Emonet-Dénand, F., Laporte, Y., Matthews, P. B. C., & Petit, J. (1977). On the subdivision of static and dynamic fusimotor actions on the primary ending of the cat muscle spindle. *Journal of Physiology*, *268*(3), 827–861. https://doi.org/10.1113/jphysiol.1977.sp011884/full

Fukami, Y. (1978). Receptor potential and spike initiation in two varieties of snake muscle spindles. *Journal of Physiology*.

Gladden, M H, & Boyd, I. A. (1985). *The Muscle Spindle*. Stockton Press. http://scholar.google.comjavascript:void(0)

Gladden, Margaret H. (1976). Structural Features relative to the Function of Intrafusal Muscle Fibres in the Cat. In *Progress in Brain Research* (Vol. 44, pp. 51–59). Elsevier. https://doi.org/10.1016/S0079-6123(08)60722-0

Haftel, V. K., Bichler, E. K., Nichols, T. R., Pinter, M. J., & Cope, T. C. (2004). Movement Reduces the Dynamic Response of Muscle Spindle Afferents and Motoneuron Synaptic Potentials in Rat. *Journal of Neurophysiology*, *91*(5), 2164–2171. https://doi.org/10.1152/jn.01147.2003

Hasan, Z. (1983). A model of spindle afferent response to muscle stretch. *Journal of Neurophysiology*, *49*(4), 989–1006. https://doi.org/10.1152/jn.1983.49.4.989

Hasan, Z., & Houk, J. C. (1975). Transition in sensitivity of spindle receptors that occurs when muscle is stretched more than a fraction of a millimeter. *Journal of Neurophysiology*, *38*(3), 673–689. https://doi.org/10.1152/jn.1975.38.3.673

Houk, J. C., Rymer, W. Z., & Crago, P. E. (1981). Dependence of dynamic response of spindle receptors on muscle length and velocity. *Journal of Neurophysiology*, *46*(1), 143–166. https://doi.org/10.1152/jn.1981.46.1.143

Housley, S. N., Nardelli, P., Powers, R. K., Rich, M. M., & Cope, T. C. (2020). Chronic defects in intraspinal mechanisms of spike encoding by spinal motoneurons following chemotherapy. *Experimental Neurology*, *331*, 113354. https://doi.org/10.1016/j.expneurol.2020.113354

Hulliger, M., Matthews, P. B., & Noth, J. (1977). Effects of combining static and dynamic fusimotor stimulation on the response of the muscle spindle primary ending to sinusoidal stretching. *The Journal of Physiology*, *267*(3), 839–856. https://doi.org/10.1113/jphysiol.1977.sp011840

Hunt, C. C., & Ottoson, D. (1975a). Impulse activity and receptor potential of primary and secondary endings of isolated mammalian muscle spindles. *The Journal of Physiology*, *252*(1), 259–281.

Hunt, C. C., & Ottoson, D. (1975b). Impulse activity and receptor potential of primary and secondary endings of isolated mammalian muscle spindles. *The Journal of Physiology*, *252*(1), 259–281. https://doi.org/10.1113/jphysiol.1975.sp011143

Hunt, C. C., & Wilkinson, R. S. (1980). An analysis of receptor potential and tension of isolated cat muscle spindles in response to sinusoidal stretch. *Journal of Physiology*. https://physoc.onlinelibrary.wiley.com/doi/abs/10.1113/jphysiol.1980.sp013240

Hunt, C. C., Wilkinson, R. S., & Fukami, Y. (1978). Ionic basis of the receptor potential in primary endings of mammalian muscle spindles. *Journal of General Physiology*. http://jgp.rupress.org/content/71/6/683.abstract

Husmark, I., & Ottoson, D. (1971). Ionic effects on spindle adaptation. *Journal of Physiology*.

Jami, L. (1992). Golgi tendon organs in mammalian skeletal muscle: Functional properties and central actions. *Physiological Reviews*, *72*(3), 623–666. https://doi.org/10.1152/physrev.1992.72.3.623

Jami, L., Murthy, K. S., & Petit, J. (1982). A quantitative study of skeletofusimotor innervation in the cat peroneus tertius muscle. *The Journal of Physiology*, *325*(1), 125–144.

Jami, L., & Petit, J. (1979). Dynamic and static responses of primary and secondary spindle endings of the cat peroneus tertius muscle [proceedings]. *Journal of Physiology*, *296*, 109P.

Jansen, J. K. S., & Matthews, P. B. C. (1962). The Effects of Fusimotor Activity on the Static Responsiveness of Primary and Secondary Endings of Muscle Spindles in the Decerebrate Cat. *Acta Physiologica Scandinavica*, *55*(4), 376–386. https://doi.org/10.1111/j.1748-1716.1962.tb02451.x

Kruse, M. N., & Poppele, R. E. (1991). Components of the dynamic response of mammalian muscle spindles that originate in the sensory terminals. *Experimental Brain Research*, *86*(2), 359–366.

Lakie, M., & Campbell, K. S. (2019). Muscle thixotropy-where are we now? *Journal of Applied Physiology (Bethesda, Md.: 1985)*, *126*(6), 1790–1799. https://doi.org/10.1152/japplphysiol.00788.2018

Lewis, D. M., & Proske, U. (1972). The effect of muscle length and rate of fusimotor stimulation on the frequency of discharge in primary endings from muscle spindles in the cat. *Journal of Physiology*, *222*(3), 511–535.

Lin, C.-C. K., & Crago, P. E. (2002). Structural model of the muscle spindle. *Annals of Biomedical Engineering*, *30*(1), 68–83. https://doi.org/10.1114/1.1433488

Lin, D. C., McGowan, C. P., Blum, K. P., & Ting, L. H. (2019). Yank: The time derivative of force is an important biomechanical variable in sensorimotor systems. *The Journal of Experimental Biology*, *222*(Pt 18). https://doi.org/10.1242/jeb.180414

Luu, B. L., Day, B. L., Cole, J. D., & Fitzpatrick, R. C. (2011). The fusimotor and reafferent origin of the sense of force and weight. *The Journal of Physiology*, *589*(Pt 13), 3135–3147. https://doi.org/10.1113/jphysiol.2011.208447

Maas, H., Gregor, R. J., Hodson-Tole, E. F., Farrell, B. J., & Prilutsky, B. I. (2009). Distinct muscle fascicle length changes in feline medial gastrocnemius and soleus muscles during slope walking. *Journal of Applied Physiology (Bethesda, Md.: 1985)*, *106*(4), 1169–1180. https://doi.org/10.1152/japplphysiol.01306.2007

Mann, C. K., Lee, L. C., Campbell, K. S., & Wenk, J. F. (2020). Force-dependent recruitment from myosin OFF-state increases end-systolic pressure–volume relationship in left ventricle. *Biomechanics and Modeling in Mechanobiology*. https://doi.org/10.1007/s10237-020-01331-6

Matthews, P. B. C. (1963a). The response of de-efferented muscle spindle receptors to stretching at different velocities. *The Journal of Physiology*, *168*(3), 660–678. https://doi.org/10.1113/jphysiol.1963.sp007214

Matthews, P. B. C. (1963b). The response of de-efferented muscle spindle receptors to stretching at different velocities. *The Journal of Physiology*, *168*(3), 660–678. https://doi.org/10.1113/jphysiol.1963.sp007214

Matthews, P. B., & Stein, R. B. (1969). The sensitivity of muscle spindle afferents to small sinusoidal changes of length. *The Journal of Physiology*, *200*(3), 723–743. https://doi.org/10.1113/jphysiol.1969.sp008719

Matthews, Peter B. C. (1981). Muscle spindles: Their messages and their fusimotor supply. *Comprehensive Physiology*.

Meyer, G. A., & Lieber, R. L. (2011). Elucidation of extracellular matrix mechanics from muscle fibers and fiber bundles. *Journal of Biomechanics*, *44*(4), 771–773. https://doi.org/10.1016/j.jbiomech.2010.10.044

Meyer, G., & Lieber, R. L. (2018). Muscle fibers bear a larger fraction of passive muscle tension in frogs compared with mice. *Journal of Experimental Biology*, *221*(22), jeb182089–5. https://doi.org/10.1242/jeb.182089

Mileusnic, M. P., Brown, I. E., Lan, N., & Loeb, G. E. (2006). Mathematical models of proprioceptors. I. Control and transduction in the muscle spindle. *Journal of Neurophysiology*, *96*(4), 1772–1788. https://doi.org/10.1152/jn.00868.2005

Nichols, T. R., & Cope, T. C. (2004). Cross-bridge mechanisms underlying the history-dependent properties of muscle spindles and stretch reflexes. *Canadian Journal of Physiology and Pharmacology*, *82*(8–9), 569–576. https://doi.org/10.1139/y04-074

Nishikawa, K. C., Monroy, J. A., Uyeno, T. E., Yeo, S. H., Pai, D. K., & Lindstedt, S. L. (2012). Is titin a 'winding filament'? A new twist on muscle contraction. *Proceedings of the Royal Society B: Biological Sciences*, *279*(1730), 981–990. https://doi.org/10.1098/rspb.2011.1304

Poppele, R. E., Kennedy, W. R., & Quick, D. C. (1979). A determination of static mechanical properties of intrafusal muscle in isolated cat muscle spindles. *Neuroscience*. https://www.sciencedirect.com/science/article/pii/0306452279901039

Poppele, R., & Quick, D. (1985). Effect of intrafusal muscle mechanics on mammalian muscle spindle sensitivity. *The Journal of Neuroscience*, *5*(7), 1881–1885. https://doi.org/10.1523/JNEUROSCI.05-07-01881.1985

Prochazka, A, & Gorassini, M. (1998). Models of ensemble firing of muscle spindle afferents recorded during normal locomotion in cats. *Journal of Physiology*. https://physoc.onlinelibrary.wiley.com/doi/abs/10.1111/j.1469-7793.1998.277bu.x

Prochazka, A., Westerman, R. A., & Ziccone, S. P. (1976). Discharges of single hindlimb afferents in the freely moving cat. *Journal of Neurophysiology*, *39*(5), 1090–1104. https://doi.org/10.1152/jn.1976.39.5.1090

Prochazka, A., Westerman, R. A., & Ziccone, S. P. (1977). Ia afferent activity during a variety of voluntary movements in the cat. *The Journal of Physiology*, *268*(2), 423–448.

Prochazka, Arthur. (2015). Proprioceptor Models. In D. Jaeger & R. Jung (Eds.), *Encyclopedia of Computational Neuroscience* (pp. 2501–2518). Springer. https://doi.org/10.1007/978-1-4614-6675-8_644

Prochazka, Arthur, & Ellaway, P. (2012). *Sensory Systems in the Control of Movement* (Vol. 2). American Cancer Society. https://doi.org/10.1002/cphy.c100086

Prochazka, Arthur, & Gorassini, M. (1998). Ensemble firing of muscle afferents recorded during normal locomotion in cats. *The Journal of Physiology*, *507*(1), 293–304.

Proske, U., & Gregory, J. E. (1977). The time-course of recovery of the initial burst of primary endings of muscle spindles. *Brain Research*, *121*(2), 358–361. https://doi.org/10.1016/0006-8993(77)90159-7

Proske, U., Morgan, D. L., & Gregory, J. E. (1992). Muscle history dependence of responses to stretch of primary and secondary endings of cat soleus muscle spindles. *The Journal of Physiology*, *445*, 81–95. https://doi.org/10.1113/jphysiol.1992.sp018913

Proske, U., & Stuart, G. J. (1985). The initial burst of impulses in responses of toad muscle spindles during stretch. *The Journal of Physiology*, *368*, 1–17. https://doi.org/10.1113/jphysiol.1985.sp015843

Proske, Uwe, & Gandevia, S. C. (2012). The proprioceptive senses: Their roles in signaling body shape, body position and movement, and muscle force. *Physiological Reviews*, *92*(4), 1651–1697.

Proske, Uwe, Tsay, A., & Allen, T. (2014). Muscle thixotropy as a tool in the study of proprioception. *Experimental Brain Research*, *232*(11), 3397–3412. https://doi.org/10.1007/s00221-014-4088-5

Savage, G., Allen, T. J., & Proske, U. (2015). The senses of active and passive forces at the human ankle joint. *Experimental Brain Research*, *233*(7), 2167–2180. https://doi.org/10.1007/s00221-015-4287-8

Schaafsma, A., Otten, E., & Van Willigen, J. D. (1991). A muscle spindle model for primary afferent firing based on a simulation of intrafusal mechanical events. *Journal of Physiology*, *65*(6), 1297–1312. https://doi.org/10.1152/jn.1991.65.6.1297

Schäfer, S. S., & Kijewski, S. (1974). The dependency of the acceleration response of primary muscle spindle endings on the mechanical properties of the muscle. *Pflugers Archiv: European Journal of Physiology*, *350*(2), 101–122. https://doi.org/10.1007/bf00586231

Schäfer, S. S., & Schäfer, S. (1969). Die Eigenschaften einer primären Muskelspindelafferenz bei rampenförmiger Dehnung und ihre mathematische BeschreibungThe characteristic of a primary \ldots. *Pflügers Archive*. https://link.springer.com/article/10.1007/BF00587210

Song, Z., Banks, R. W., & Bewick, G. S. (2015). Modelling the mechanoreceptor's dynamic behaviour. *Journal of Anatomy*, *227*(2), 243–254. https://doi.org/10.1111/joa.12328

Taylor, A., & Cody, F. W. J. (1974). Jaw muscle spindle activity in the cat during normal movements of eating and drinking. *Brain Research*, *71*(2), 523–530. https://doi.org/10.1016/0006-8993(74)90996-2

Taylor, A., Durbaba, R., Ellaway, P. H., & Rawlinson, S. (2000). Patterns of fusimotor activity during locomotion in the decerebrate cat deduced from recordings from hindlimb muscle spindles. *The Journal of Physiology*, *522*(3), 515–532.

Taylor, A., Ellaway, P. H., & Durbaba, R. (1999). *Why are there three types of intrafusal muscle fibers?* (Vol. 123, pp. 121–131). Elsevier.

Taylor, Anthony, Durbaba, R., Ellaway, P. H., & Rawlinson, S. (2006). Static and dynamic γ-motor output to ankle flexor muscles during locomotion in the decerebrate cat. *The Journal of Physiology*, *571*(3), 711–723.

Thornell, L.-E., Carlsson, L., Eriksson, P.-O., Liu, J.-X., Österlund, C., Stål, P., & Pedrosa-Domellöf, F. (2015a). Fibre typing of intrafusal fibres. *Journal of Anatomy*, *227*(2), 136–156. https://doi.org/10.1111/joa.12338

Thornell, L.-E., Carlsson, L., Eriksson, P.-O., Liu, J.-X., Österlund, C., Stål, P., & Pedrosa-Domellöf, F. (2015b). Fibre typing of intrafusal fibres. *Journal of Anatomy*, *227*(2), 136–156. https://doi.org/10.1111/joa.12338

Vallbo, A. B. (1974). Human muscle spindle discharge during isometric voluntary contractions. Amplitude relations between spindle frequency and torque. *Acta Physiologica Scandinavica*, *90*(2), 319–336.

Vincent, J. A., Wieczerzak, K. B., Gabriel, H. M., Nardelli, P., Rich, M. M., & Cope, T. C. (2016). A novel path to chronic proprioceptive disability with oxaliplatin: Distortion of sensory encoding. *Neurobiology of Disease*, *95*, 54–65. https://doi.org/10.1016/j.nbd.2016.07.004

SUPPLEMENTAL FIGURES AND LEGENDS

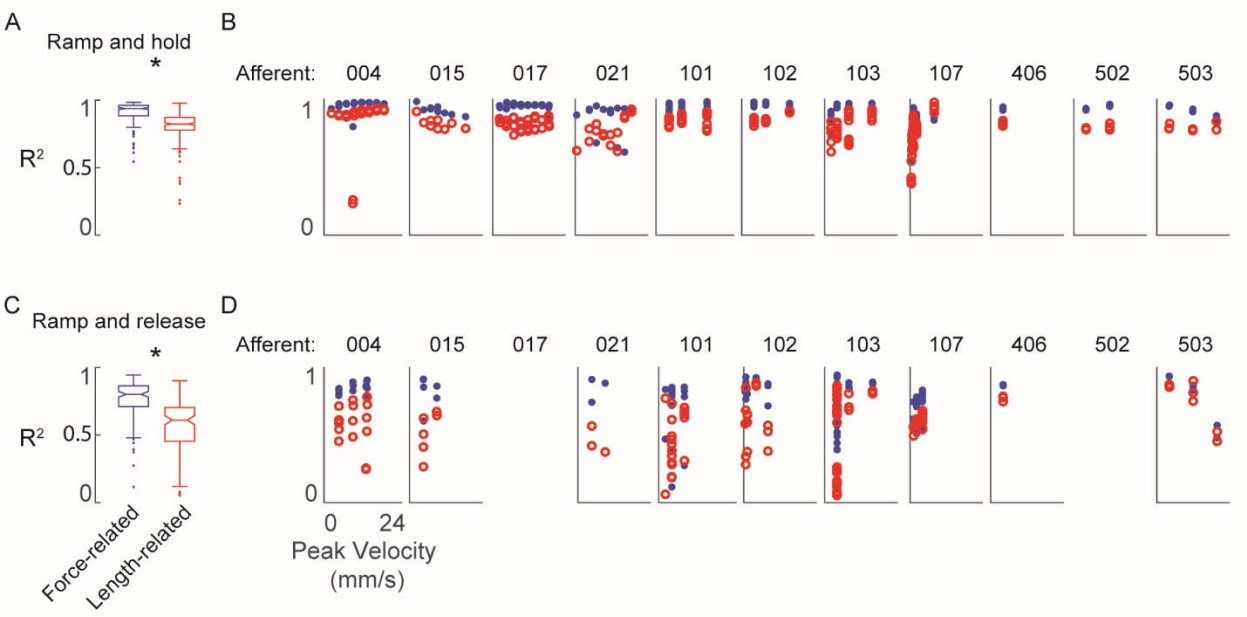

Figure S1 Goodness-of-fit to measured muscle spindle Ia afferent firing rates using estimated muscle fiber force and yank (blue) compared to kinematics model (red) as baseline comparison. A) Box and whisker plots of model goodness of fit (R^2) for all ramp-and-hold trials using estimated fiber force-based (blue) versus length-based (red) models. * denotes a significant difference between the model goodness of fit based on cumulative squared errors; $p<0.05$, one-way ANOVA. B) R^2 values for all individual trials of ramp-and-hold and within each afferent plotted versus stretch velocity for force-based (blue dots) versus length-based (red dots) models. C-D) Same as A-B, only for repeated ramp-release trials.

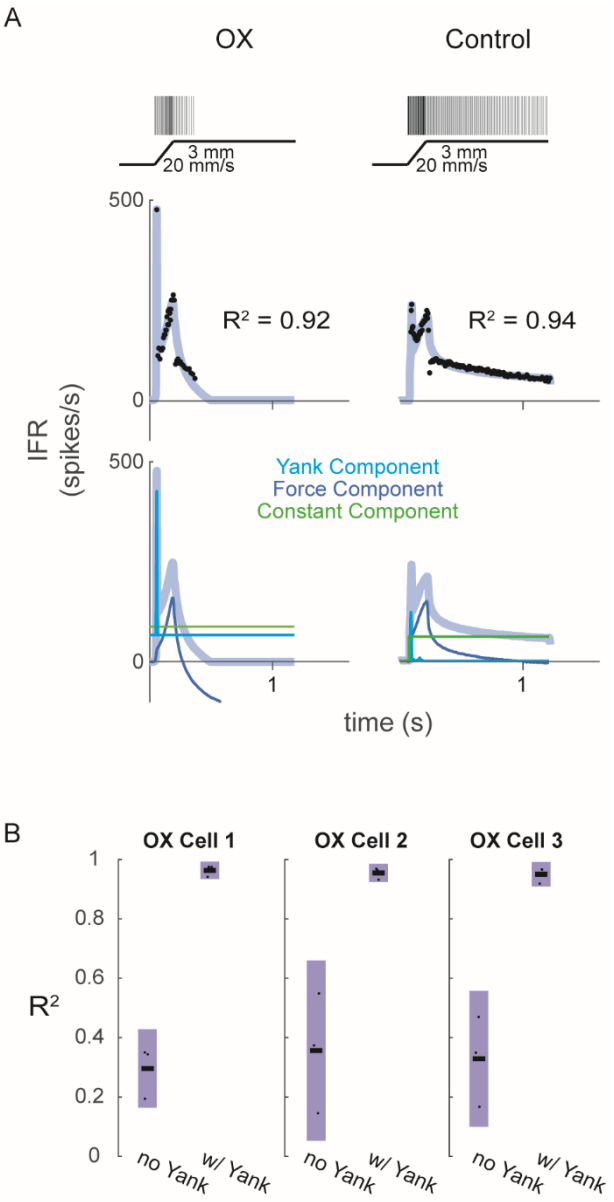

Figure S2

Fits of muscle spindle firing rates before and after oxaliplatin-induced neuropathy using estimated muscle fiber force and yank. (A) Example Ia afferent responses to stretch and force-based model fits. Left column shows a typical Ia afferent response to a ramp-hold stretch applied to the triceps surae of a rat treated with oxaliplatin chemotherapy (Bullinger et al. 2011). Right column shows typical response of Ia afferent in response to same ramp-hold stretch. Raster plots indicate times at which action potentials are recorded and are shown above imposed stretches. Below are the IFR and corresponding model fits shown above the same model fits with their respective components. (B) Variance of muscle spindle Ia afferent responses accounted for by force related model with (right bar in each plot) and without (left bar in each plot) yank for 3 Ia afferents from 3 oxaliplatin-treated rats. Black horizontal bars represent the means, blue bars represent the standard deviations, and black dots represent the data points from each trial (3 trials per afferent).

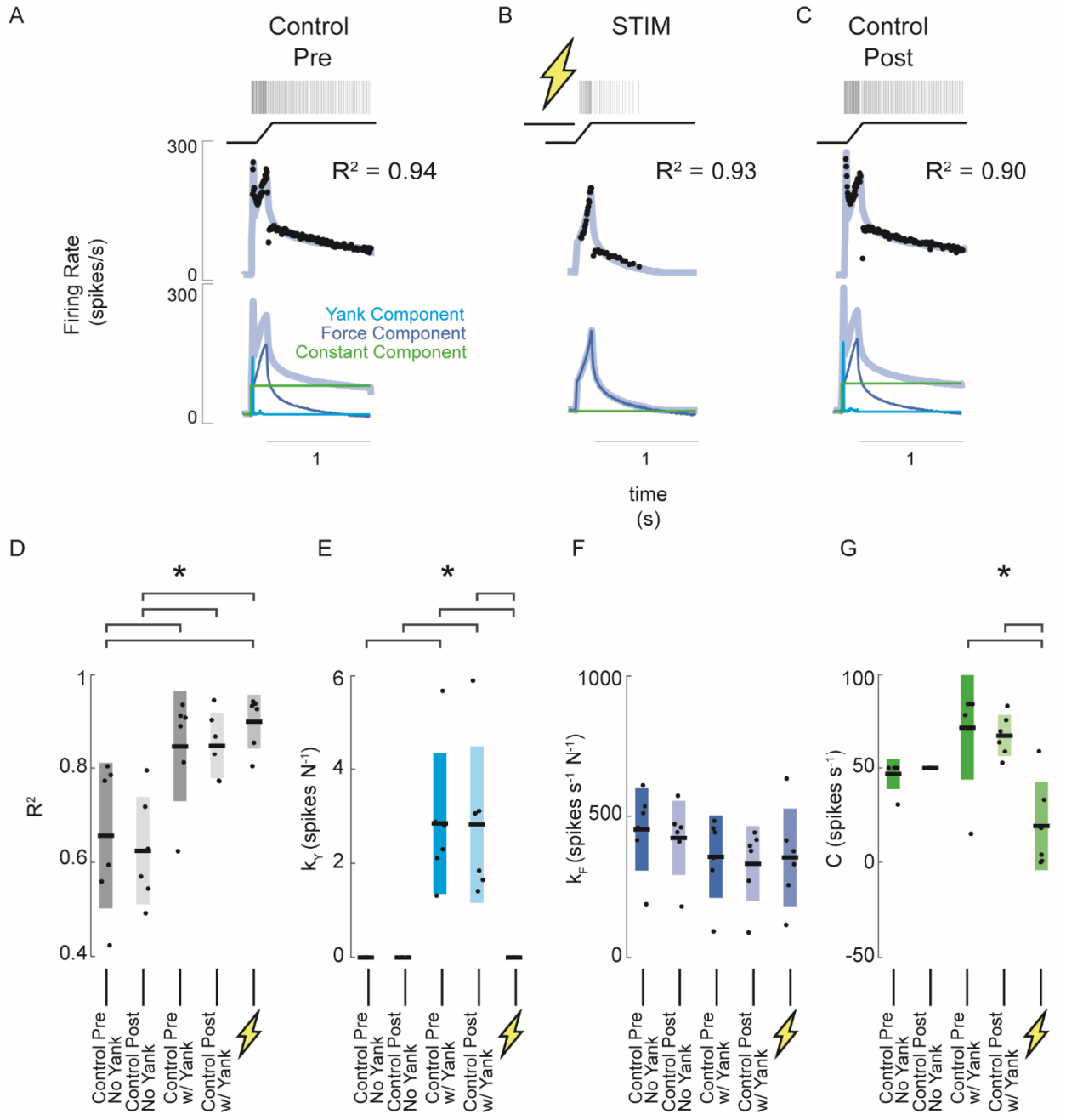

Figure S3

Estimated muscle fiber force-related model predicts changes in muscle spindle encoding caused by axonal stimulation. (A) Example of pre-stimulus control trial consisting of a 3 mm ramp-hold stretch at 20 mm/s. Raster represents the times of recorded action potentials in response to the ramp-hold stimulus shown directly below it. Black dots represent the afferent IFR corresponding to the raster. The gray-blue line represents the model prediction using force, yank, and constant components. Below this are the same model prediction as above (grey-blue) and model prediction components (blue – force component; cyan – yank component; green – constant component). (B) Example of stimulus trial consisting of the same stretch applied as A, with a train of antidromic action potentials induced by suprathreshold current injection into the Ia axon prior to stretch. The model fit in this trial represents the best fit without the yank component.

Notice the quality of fit does is roughly equal in this trial with that of the pre-stimulus trial in A, but no yank component was necessary. (C) Example of post-stimulus control trial. Same stretch and model components were used as in A. (D) Goodness of fit (R^2) of force-related model for 6 afferents subjected to the same trials as shown in A-C. The first two columns show R^2 values of the model fits without yank components for the pre- and post-stimulus control trials, respectively, for all 6 afferents. The third and fourth columns from the left show R^2 values for the model fits with yank components for the pre- and post-stimulus control trials, respectively, for the same 6 afferents. The fifth column shows R^2 values for the model fits for the stimulus trials. This model did not use a yank component. (E) Model sensitivity to yank for the same model fits and afferents as D. (F) Model sensitivity to force for the same model fits and afferents as D and E. (G) Model constant component for the same model fits and afferents as D-F. Brackets above plots indicate significant differences between the means ($p < 0.05$).

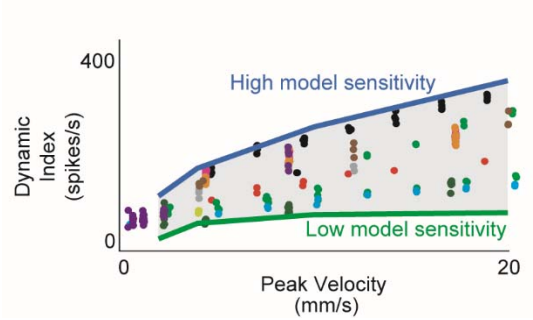

Figure S4

Estimated muscle fiber force model predicts inter-afferent variability of healthy afferent firing properties across perturbation velocity and acceleration. (A) Same dynamic index data shown in Figure 3-2 (colored dots) with predicted range of dynamic indices from model (gray shaded area). Nominal simulations were performed with the same force and yank model sensitivities for 4 stretch trials (2, 4, 10, 20 mm/s) from the same animal. Model parameter sweeps were performed for force and yank sensitivities for each of the 4 trials from 0.1 to 5 times the nominal value for each parameter. Green line represents the minimum dynamic indices from each of the 4 parameter sweeps from trials for which there was a spiking response (usually corresponding to low force and yank sensitivities). Blue line represents maximum dynamic indices from each of the 4 parameter sweeps (usually corresponding to high force and yank sensitivities). Gray shaded area represents plausible space of simulated dynamic index.

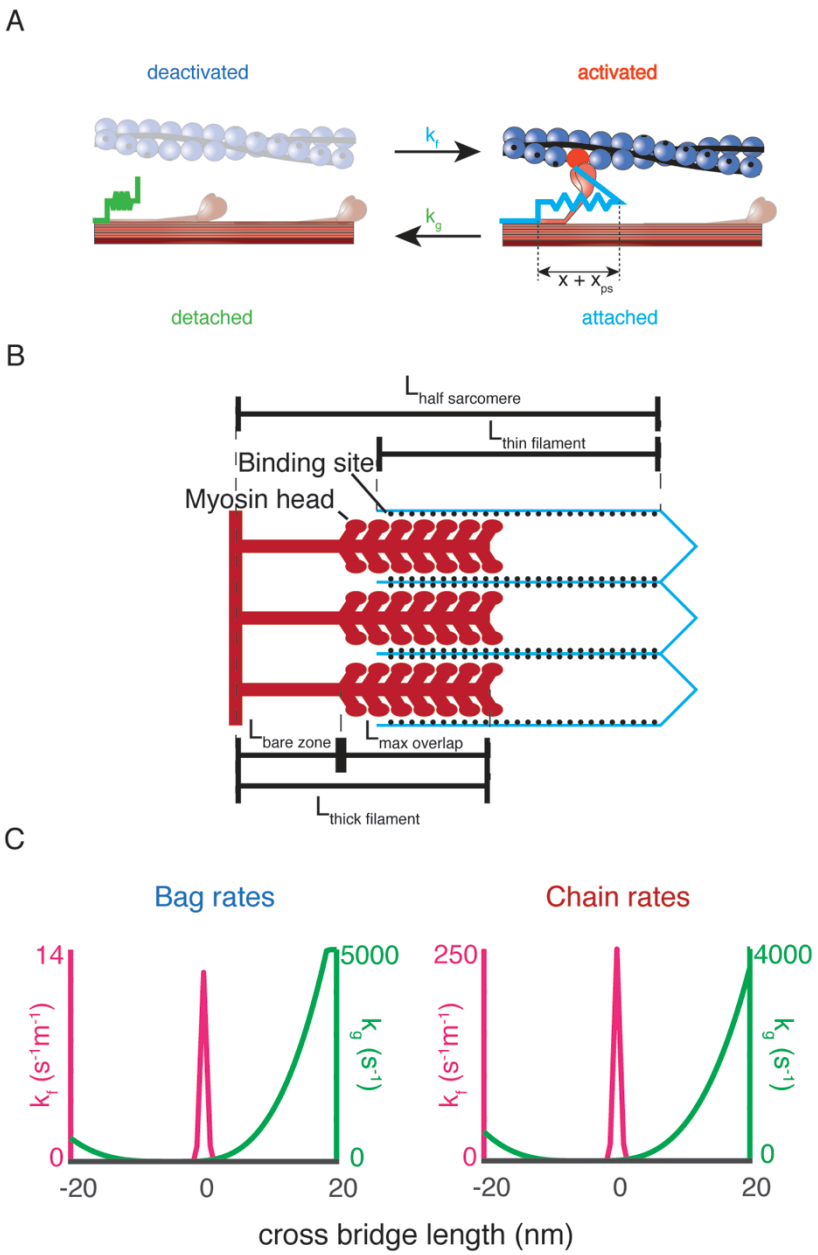

Figure S5

Biophysical intrafusal muscle models. A) Two-state dynamic system of cross-bridge cycling. A population of detached cross-bridges attaches at rate $k_f(x)$, and the population of attached cross-bridges detaches at rate $k_g(x)$. When a cross-bridge is formed at length x, an additional "powerstroke" length, x_{ps}, is applied to the cross-bridge to generate a contractile force. B) Schematic of length variables accounted for in muscle model. The amount of overlap between the myosin heads of the thick filament (red) and actin binding sites of the thin filament (blue lines, black dots) is the relevant variable for the simulations. The fraction of overlap is simply the difference between the total length of the thick and thin filaments with the length of the half sarcomere, expressed as a fraction of the maximum potential overlap. C) Rate equations for myosin dynamics. The rate at which detached myosin

heads will attach as a function of the length, $k_f(x)$ of attachment is a Gaussian function, centered around 0 nm (shown in blue). The rate at which attached cross-bridges will detach as a function of their length $k_g(x)$ is an offset polynomial function (shown in orange).

Parameter	Value (dynamic, static fiber)	Units	Description
k_{cb}	1	mN m^{-1}	Unit cross-bridge stiffness
x_{ps}	2.5	nm	Unit power stroke distance
$L_{thick\ filament}$	815	nm	Length of thick filament
$L_{thin\ filament}$	1120	nm	Length of thin filament
$L_{bare\ zone}$	80	nm	Length of bare zone
$c_{filament}$	0.5	-	Filament compliance factor
ρ_{cb}	6.9 $\times 10^{16}$	m^{-2}	Cross-bridge number density
l_0	1050, 1200	nm	Passive force reference length
k_{pas}	100, 250	N m^{-2} nm^{-1}	Passive force linear stiffness

Table S1
Constant parameters used in both dynamic and static intrafusal muscle fiber models. These parameters did not change in any simulation presented in this study. When two values are presented, they represent the respective values for the dynamic and static fibers.